Lithos 155 (2012) 256–271

Contents lists available at SciVerse ScienceDirect

Lithos

journal homepage: www.elsevier.com/locate/lithos

Petrology, geochemistry and Re–Os isotopes of peridotite xenoliths from Yantai, Shandong Province: Evidence for Phanerozoic lithospheric mantle beneath eastern North China Craton

Lu-Bing Hong [a,b], Yi-Gang Xu [a,*], Zhong-Yuan Ren [a], Yong-Sheng Kuang [a,b,c], Ya-Ling Zhang [a,b], Jie Li [a], Fang-Yue Wang [a,b], Hong Zhang [a,b]

[a] State Key Laboratory of Isotope Geochemistry, Guangzhou Institute of Geochemistry, Chinese Academy of Sciences, Guangzhou 510640, China
[b] University of Chinese Academy of Sciences, Beijing 100049, China
[c] Geological Survey Institute of Guangdong Nonferrous Metals Geological Survey Bureau, Guangzhou 510800, China

ARTICLE INFO

Article history:
Received 2 June 2012
Accepted 15 September 2012
Available online 25 September 2012

Keywords:
Mantle xenoliths
Polybaric melting
Phanerozoic lithosphere
Yantai
Shandong
North China Craton

ABSTRACT

Petrology, geochemistry and Re–Os isotopes of peridotite xenoliths from Yantai (Shandong Province) are reported in this paper with aims of constraining the age and evolution of the lithospheric mantle beneath eastern North China Craton. The Yantai xenoliths contain predominant harzburgites and subordinate lherzolites. Although their highly incompatible element compositions have been modified by metasomatism, the heavy rare earth element (REE) and Y contents in the Yantai peridotites are primarily governed by partial melting, which started in garnet stability field then continued in spinel stability field after breakdown of garnet to two pyroxenes and spinel. Such a polybaric melting produced a residual mantle in which degree of depletion decreases with depth. Os isotopic ratios of the most refractory peridotites (Al_2O_3<1.2 wt.%) range from 0.117 to 0.126, yielding T_{RD} model ages between 0.5 and 1.7 Ga. This suggests co-existence of Phanerozoic and Proterozoic mantle beneath Shandong Province. Alternatively, the whole lithospheric mantle beneath Yantai was likely formed during the Phanerozoic, given the resemblance of their Os isotopic ratios with those of abyssal peridotites. The latter interpretation is consistent with the fact that all the studied samples plot along the oceanic trend in a plot of forsterite content in olivine versus olivine mode. It also gains further support from the contrasting ε_{Nd} between the late Mesozoic lithospheric mantle and Cenozoic mantle beneath the region. The data presented in this study therefore argue for a complete replacement of the cratonic mantle by upwelling asthenosphere.

1. Introduction

Recent studies have shown that the Archean North China Craton (NCC) experienced thermo-tectonic reactivation during the Mesozoic, resulting in replacement of the old, cold, thick and refractory lithospheric keel by young, hot, thin and fertile asthenospheric mantle (Fan et al., 2000; Gao et al., 2002; Griffin et al., 1998; Menzies and Xu, 1998; Menzies et al., 1993; Xu, 2001). This recognition highlights that the cratonic lithospheric mantle is not preserved forever and can be destroyed under certain circumstances, especially when water is involved (Menzies et al., 2007; Niu, 2005; Zhu et al., 2011). It also significantly promotes our understanding of intraplate deformation and magmatism.

The idea of the destruction of the NCC was largely built on the geology of Shandong Province where a variety of mafic magmas of different ages are present. In particular, the mantle xenoliths entrained by the Ordovician diamondiferous kimberlites and late Cenozoic alkali basalts in this same area provide the direct samples for the contrasting nature and age of the sub-continental lithospheric mantle (SCLM) during the Paleozoic and the present time (e.g., Chu et al., 2009; Fan et al., 2000; Gao et al., 2002; Griffin et al., 1998; Menzies et al., 1993; Zhang et al., 2008; Zheng, 2009). Another prominent feature of the regional geology is the NNE-oriented Tanlu trans-lithospheric fault (Fig. 1a), which is considered as the locus of lithospheric thinning (Chen, 2010; Menzies et al., 2007; Xiao et al., 2010; Zheng et al., 1998). Studies of xenoliths show that the Tanlu fault is associated with sheared peridotites (e.g., Xu et al., 1996), and deformation and melt ingress are inextricably linked (e.g., Xiao et al., 2010; Zheng et al., 1998). Perhaps the very tectonic processes that triggered crack propagation allowed for concomitant melt formation. At some stage the lowermost lithosphere must have been warmed conductively by

* Corresponding author. Tel.: +86 20 8529 0109; fax: +86 20 8529 0261.
E-mail address: yigangxu@gig.ac.cn (Y.-G. Xu).

0024-4937/$ – see front matter © 2012 Elsevier B.V. All rights reserved.
http://dx.doi.org/10.1016/j.lithos.2012.09.005

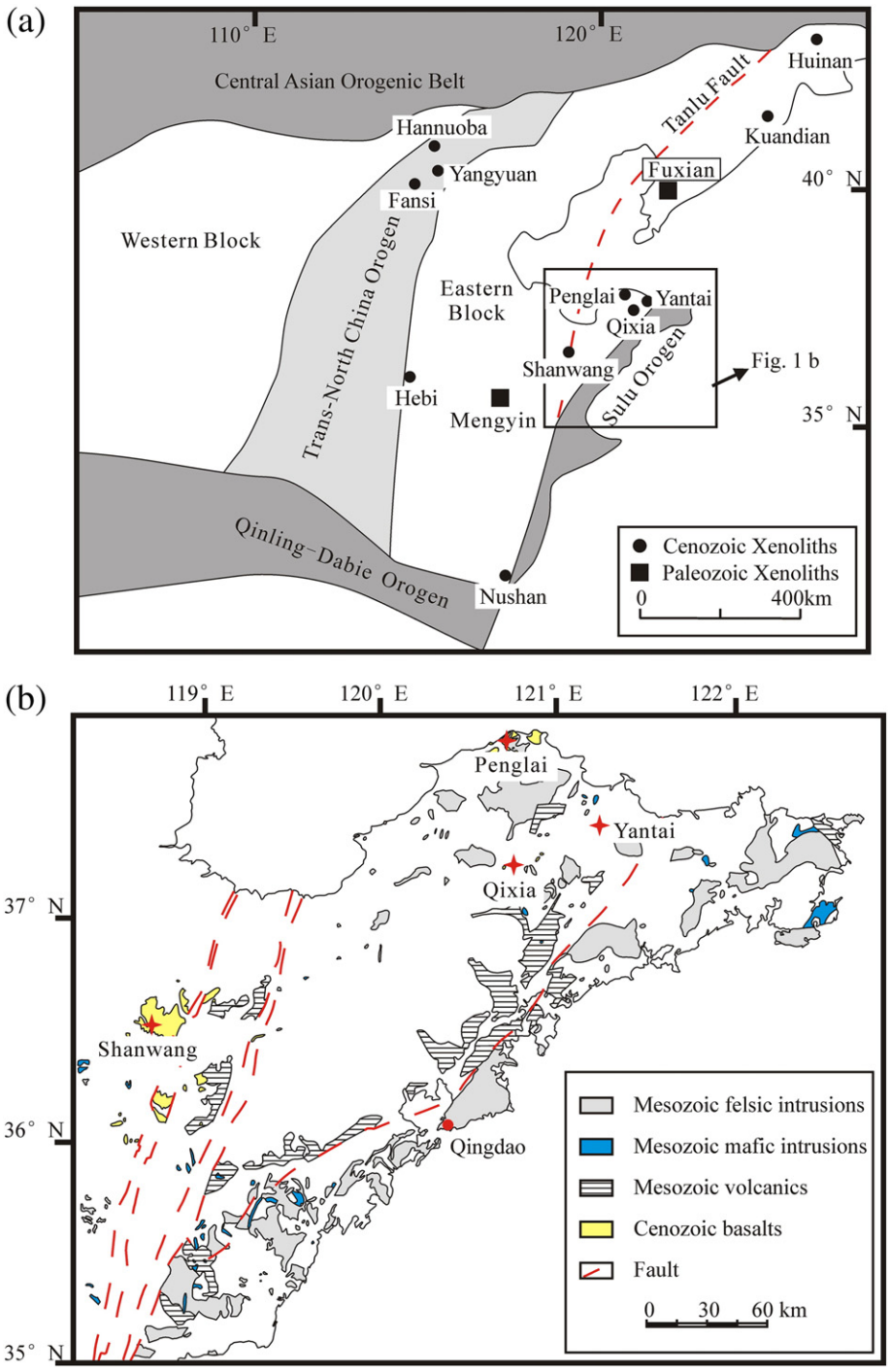

Fig. 1. (a) Simplified geological map of North China Craton; (b) distribution of Mesozoic to Cenozoic igneous rocks and xenolith location in Shandong Peninsula. Tectonic subdivisions are based on Zhao et al. (2001).

heat transported from the vigorously upwelling asthenosphere by melts (Menzies et al., 2007). This is supported by recent seismic investigations, which reveals a thin lithosphere underneath the Tanlu fault (Chen, 2010).

If the Tanlu fault is the locus of asthenospheric ascent, its underlying lithospheric mantle would be fully made of newly accreted mantle. Many investigations on the age and composition of mantle peridotites have been carried out in recent years in order to test this proposition (e.g., Chu et al., 2009; Fan et al., 2000; Gao et al., 2002; Xiao et al., 2010; Zheng et al., 1998), but the architecture of the lithospheric mantle beneath Shandong Province remains a subject of debate. Some researchers believe that ancient SCLM survives the replacement process (e.g., Xiao et al., 2010; Zheng et al., 1998), on the basis of occurrence of highly refractory peridotites, especially in the area away from the Tanlu fault. The others claimed that the entire SCLM beneath Shandong was formed during the Phanerozoic (e.g., Chu et al., 2009; Gao et al., 2002), probably as a result of lithospheric thinning and accretion (Xu et al., 2004a). In their model, the ancient Os model ages are attributed to the heterogeneity of Os isotope in convective mantle (Chu et al., 2009).

The disputation concerns the geological significance of Os model age and whether refractoriness of peridotites is age-dependent. To address these questions, we focused on a suite of refractory peridotite xenoliths newly discovered in the Pailou Cenozoic volcanic field, near

Yantai in the Shandong Peninsula. The petrological, geochemical and Os isotopic data are integrated in this study to discuss the age and evolution of the lithospheric mantle in Shandong Peninsula. This, together with previously published data, enables us to outline the spatial heterogeneity and evolution of the SCLM beneath Shandong Province.

2. Geological background and xenolith petrography

The North China Craton is one of the oldest nuclei in the world (e.g., Liu et al., 1992). Based on the geochronology, lithological assemblage and tectonic evolution, the basement of the NCC can be divided into three units, namely Eastern and Western Block, and the Paleoproterozoic Trans-North China Orogen, separating the former two from each other (Fig. 1a; Zhao et al., 2001). The basement of the Eastern and Western Blocks are similar and are predominantly composed of Early to Late Archean tonalite–trondhjemite–granodiotite (i.e., TTG). The Trans-North China Orogen is primarily composed of Late Archean to Paleoproterozoic basement rocks metamorphosed at greenschist to granulite facies due to the collision between the Eastern and Western Blocks at ~1.8 Ga (Zhao et al., 2001).

Since the amalgamation of Eastern Block and Western Block into an integrated craton, the NCC had been stable until kimberlites erupted in Early Paleozoic at Mengyin in west Shandong and Fuxian in Liaoning Peninsula (Fig 1a). Studies on peridotites captured in these two kimberlites suggest a thick (>180 km), cold (<40 mW/m^2), old (most of Os model ages >2.5 Ga) and refractory SCLM beneath NCC during Early Paleozoic (e.g., Gao et al., 2002; Griffin et al., 1998; Menzies et al., 1993). Since Mesozoic, especially Late Mesozoic, the NCC was destabilized, as expressed by intense magma activities ranging from late Mesozoic to Cenozoic (Xu et al., 2009; and references therein). The mantle xenoliths entrained by Cenozoic basalts reveal that Cenozoic SCLM beneath Eastern NCC is thin (<80 km), hot (~65 mW/m^2), young and fertile (Fan et al., 2000; Gao et al., 2002; Rudnick et al., 2004; Xu and Bodinier, 2004; Zheng et al., 1998). This suggests a removal of >100 km of Archean lithosphere during Phanerozoic (Griffin et al., 1998; Menzies et al., 1993).

Shandong Province, located in the central part of the eastern NCC, is separated by the Tanlu fault into two parts (Fig. 1). The western part is called Luxi where the Ordovician diamondiferous kimberlites are situated, and the eastern part is the Shandong Peninsula. Cenozoic basalts in Shandong are mainly distributed along Tanlu fault and in the

Table 1
Mineral modal compositions, and major and trace element compositions of whole rock from Yantai peridotites.

	Lherzolite			Harzburgite									
	ML-3	ML-4	ML-5	ML-1	ML-2	ML-8	ML-9	ML-10	ML-11	ML-12	ML-13	ML-14	ML-15
Mineral modal (%)													
Ol		57.2	60.0	74.7	78.9	77.3	68.2	79.7	78.5		68.6	78.3	83.2
Opx		26.9	12.5	20.6	15.3	18.0	23.4	14.1	16.7		24.1	17.5	14.1
Cpx		13.4	24.0	3.5	4.9	3.7	6.3	4.7	3.2		5.8	3.4	2.0
Sp		2.5	3.1	1.3	1.2	1.1	1.5	1.5	2.0		1.9	0.7	1.1
Major element (wt.%)													
SiO_2	44.09	45.12	43.91	43.95	43.84	44.01	44.31	43.81	43.67	43.96	44.99	44.22	43.03
TiO_2	0.04	0.12	0.11	0.03	0.01	0.03	0.02	0.01	0.01	0.01	0.00	0.02	0.02
Al_2O_3	2.25	3.97	3.52	1.75	1.54	1.23	1.64	1.52	1.31	1.60	1.82	0.80	0.91
Fe_2O_3	9.08	8.59	8.69	7.97	8.28	8.74	8.79	8.29	8.71	8.90	8.54	8.70	8.48
MnO	0.13	0.12	0.12	0.12	0.11	0.12	0.13	0.11	0.12	0.13	0.12	0.13	0.12
MgO	41.46	38.61	37.79	44.92	44.68	44.56	42.64	44.69	44.95	43.61	42.71	44.69	46.46
CaO	2.42	2.92	5.29	0.97	1.24	0.99	1.66	1.24	0.84	1.53	1.56	0.92	0.66
Na_2O	0.23	0.28	0.34	0.07	0.08	0.05	0.53	0.10	0.08	0.03	0.03	0.20	0.06
K_2O	0.05	0.05	0.01	0.00	0.00	0.02	0.06	0.01	0.07	0.01	0.02	0.05	0.04
P_2O_5	0.04	0.01	0.01	0.01	0.01	0.05	0.03	0.01	0.03	0.02	0.03	0.08	0.03
L.O.I	0.11	−0.25	−0.16	−0.25	−0.30	−0.16	0.07	−0.25	0.00	0.06	−0.09	−0.02	−0.23
Total	99.90	99.55	99.63	99.55	99.50	99.64	99.86	99.55	99.80	99.86	99.71	99.78	99.57
Trace element composition(ppm)													
Sr	35.78	22.54	16.02	1.93	2.59	6.70	8.42	5.43	28.54	3.56	3.25	10.51	7.36
Ti	224.2	637.5	599.3	121.1	112.4	199.1	142.6	78.3	85.2	70.1	56.6	137.4	128
Y	1.93	3.35	4.22	0.67	0.76	0.69	0.84	0.22	0.59	0.49	0.44	0.50	0.41
Zr	4.92	6.67	2.71	0.73	0.83	3.98	4.79	6.03	1.75	0.69	0.71	3.55	3.35
Nb	2.43	0.94	0.21	0.19	0.19	1.90	1.78	0.78	1.02	0.53	0.60	1.53	1.35
Rb	1.81	0.34	0.23	0.13	0.13	0.31	1.31	0.19	0.98	0.32	0.34	1.00	0.70
Ba	3.58	1.15	0.32	0.13	0.14	1.78	2.60	0.62	7.58	0.95	0.92	3.07	2.19
La	1.97	0.94	0.29	0.06	0.08	0.47	0.39	0.26	2.05	0.10	0.23	0.57	0.59
Ce	4.58	2.10	0.82	0.17	0.21	0.88	0.68	0.51	3.77	0.18	0.35	0.99	1.01
Pr	0.62	0.27	0.14	0.03	0.03	0.11	0.08	0.06	0.39	0.02	0.04	0.13	0.11
Nd	2.47	1.05	0.80	0.12	0.16	0.39	0.28	0.24	1.32	0.08	0.14	0.49	0.41
Sm	0.49	0.29	0.33	0.04	0.05	0.08	0.06	0.05	0.21	0.02	0.02	0.09	0.08
Eu	0.17	0.12	0.13	0.02	0.02	0.03	0.02	0.02	0.06	0.01	0.01	0.03	0.03
Gd	0.47	0.42	0.50	0.07	0.08	0.09	0.08	0.05	0.18	0.04	0.03	0.09	0.08
Tb	0.07	0.08	0.10	0.01	0.02	0.02	0.02	0.01	0.02	0.01	0.01	0.01	0.01
Dy	0.39	0.56	0.72	0.10	0.12	0.11	0.13	0.05	0.12	0.07	0.05	0.08	0.07
Ho	0.08	0.13	0.16	0.03	0.03	0.02	0.03	0.01	0.02	0.02	0.02	0.02	0.01
Er	0.20	0.38	0.46	0.08	0.09	0.08	0.10	0.02	0.07	0.07	0.06	0.05	0.04
Tm	0.03	0.06	0.07	0.01	0.02	0.01	0.02	0.00	0.01	0.01	0.01	0.01	0.01
Yb	0.19	0.37	0.42	0.09	0.10	0.09	0.12	0.03	0.07	0.10	0.09	0.06	0.05
Lu	0.03	0.07	0.07	0.02	0.02	0.02	0.02	0.01	0.01	0.02	0.02	0.01	0.01
Th	0.26	0.10	0.02	0.02	0.02	0.08	0.11	0.07	0.33	0.03	0.05	0.09	0.12
U	0.07	0.02	0.01	0.01	0.01	0.05	0.04	0.02	0.07	0.02	0.02	0.08	0.05

Modal compositions are calculated from bulk compositions and constituent mineral chemistries using least-squares regression method.

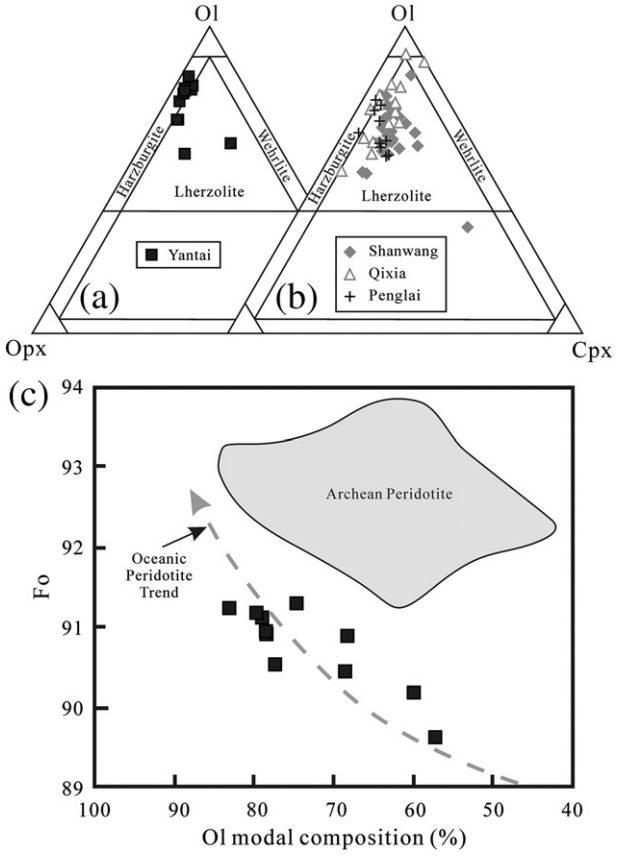

Fig. 2. (a) and (b) Modal compositions of the peridotites from Yantai and other localities in Shandong Peninsula. Note the predominance of refractory harzburgites over lherzolites in the Yantai xenolith population. Data source for Shandong peridotites: Chu et al. (2009), Rudnick et al. (2004) and Zheng et al. (1998). (c) Plot of ol modal composition vs Fo. The cratonic field and oceanic peridotite trend are after Boyd (1989). In spite of the predominance of refractory harzburgites, the Yantai peridotites follow the oceanic trend, but are distinct from Archean peridotites.

northern part of the Shandong Peninsula. Many of these Cenozoic basalts contain abundant mantle xenoliths (e.g., Shanwang, Penglai, Qixia; Fig. 1b). The peridotite xenoliths studied in this paper are collected from Yantai basalt which erupted at ~7.4 Ma (Ar–Ar age, Hong et al., unpublished data). The Yantai peridotites are fresh and anhydrous, and are composed of predominant harzburgites (with <5% cpx) and minor lherzolites (Table 1; Fig. 2a). The predominance of refractory harzburgites over lherzolites in the Yantai xenolith population is different from those observed in other localities (e.g. Shanwang, Qixia, Penglai) in Shandong, where lherzolites dominate (Fig. 2b). For the convenience of description, clinopyroxene-poor (<7% cpx) lherzolites (sample ML-9 and ML-13) are also classified into harzburgites.

The Yantai peridotites mainly show a porphyroclastic texture, which is characterized by large grains of olivine (ol) and orthopyroxene (opx) (2–5 mm) scattering in the small-sized (<2 mm) neoblasts. They often show straight boundaries, most of which are converged at 120° in triple junctions. Some samples show a greater degree of recrystallization with elongated grains and weak lineation. In some samples (sample ML-2, ML-4 and ML-5), the spongy texture of clinopyroxene (cpx) is observed (Fig. 3a). Spinels (sp) are minor and smaller, commonly with vermicular form and holly-leaf shape. They are more often concentrated on the side of opx and cpx, forming pyroxene-spinel cluster (Fig. 3b).

3. Sample preparation and analytical methods

Peridotite xenoliths were sawn into slabs and central parts were used for bulk-rock analyses. The samples were firstly crushed into small chips, and then washed with distilled water in ultrasonic bath for several times. After that, the cleaned samples were ground into a fine powder using an agate mortar. All the analyses are acquired at the State Key Laboratory of Isotope Geochemistry, Guangzhou Institute of Geochemistry, Chinese Academy of Sciences (GIG-CAS).

The mineral chemistry was obtained with a JEOL JXA-8100 Superprobe. The operating conditions are as follows: 15 kV accelerating voltage, 20 nA beam current and 1 μm beam diameter, and 10 s peak counting time for major elements (7 s for Na) and 20 s peak counting time for minor elements (such as Ni, Cr, Ti). The data reduction was carried out using ZAF correction.

Whole-rock major element compositions were carried out by X-ray fluorescence spectrometry (XRF) on fused glass disks using Rigaku ZSX-100e XRF instrument. Analytical procedure is described by Goto and Tatsumi (1996). The same samples were also analyzed for trace elements and rare-earth elements (REE) by inductively coupled plasma-mass spectrometry (ICP-MS), using techniques described by Liu et al. (1996). Precision for most trace elements was better than 10%. In situ trace element analysis of cpx was performed using an Agilent 7500a ICP-MS system coupled with a Resolution M50-HR 193 nm ArF-excimer laser sampler, following the analytical procedure described by Tu et al. (2011). Calibration was carried out externally using NIST 612 with Si as an internal standard. Repeated analyses of NIST 612 and NIST 610 indicate precision and accuracy

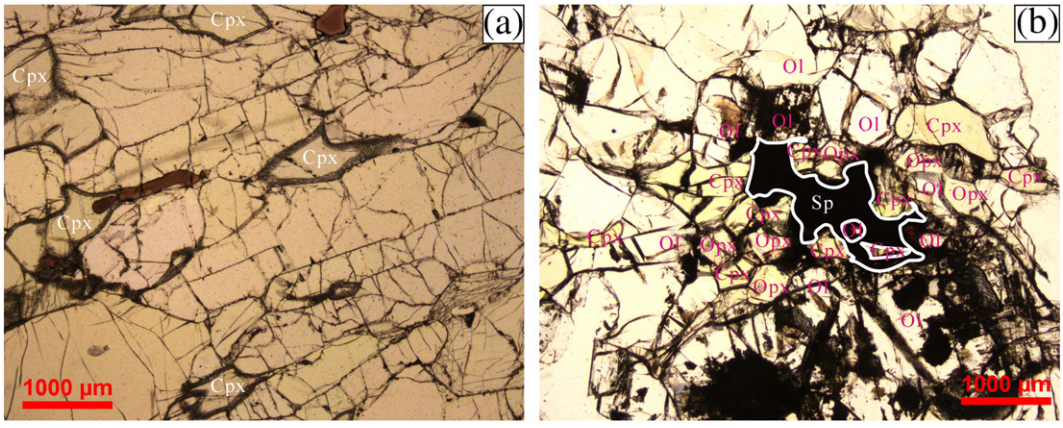

Fig. 3. Photomicrographs of the spongy texture of clinopyroxenes (a), and clusters of pyroxene and spinels (b). Both are plane-polarized light.

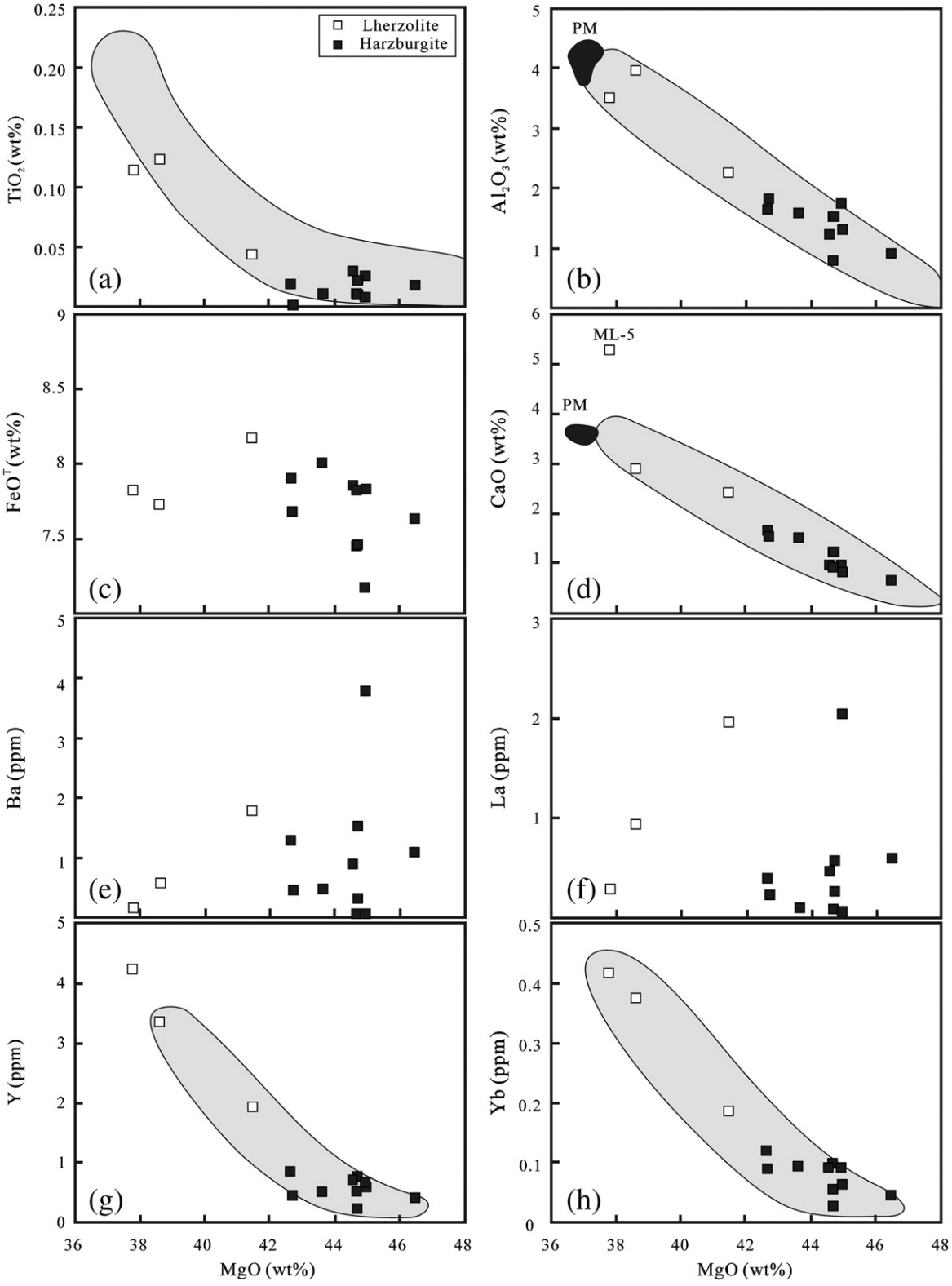

Fig. 4. Plots of TiO_2, Al_2O_3, FeO^T, CaO, Ba, La, Y and Yb contents against MgO for the Yantai peridotites. Shaded fields represent the compositional range of worldwide peridotites after Takazawa et al. (2000). Black fields represent the compositions of the primitive mantle after Jagoutz et al. (1979), and Hart and Zindler (1986).

both better than 4% for most elements. For cpx, the relative standard deviations (RSDs) of most elements are better than 15%.

Re contents were analyzed by ICP-MS, and Os contents and Os isotope ratios were determined by Triton TIMS, following the analytical procedure detailed by Li et al. (2011). Both Re and Os were corrected for blanks. Total blank levels were 11 ± 1 pg and 3 ± 1 pg for Re and Os, respectively, and the blank $^{187}Os/^{188}Os$ ratio was 0.256 ± 0.034 (Li et al., 2011). The contributions of the blanks to measured Os contents were less than 1.5% for all samples, and to Re contents were less than 30 % for most samples.

Table 2
Major element (wt.%) compositions of minerals, equilibrium temperature (°C) from Yantai peridotites.

mineral	Lherzolite								Harzburgite			
	ML-4				ML-5				ML-1			
	Ol	Opx	Cpx	Sp	Ol	Opx	Cpx	Sp	Ol	Opx	Cpx	Sp
SiO_2	41.14	55.15	52.02	0.10	40.92	55.45	52.12	0.06	41.17	55.70	53.06	0.09
TiO_2	–	0.11	0.33	0.13	0.03	0.11	0.27	0.13	–	0.05	0.09	0.13
Al_2O_3	0.03	5.58	7.30	58.25	–	4.12	5.56	54.18	0.02	4.10	4.97	45.61
Cr_2O_3	–	0.37	0.67	9.72	–	0.31	0.69	14.66	–	0.73	1.04	23.46
FeO	10.00	6.26	3.16	10.77	9.50	6.07	2.75	11.27	8.49	5.37	2.58	11.39
MnO	0.11	0.10	0.05	0.09	0.13	0.12	0.09	0.12	0.10	0.12	0.06	0.12
MgO	48.39	31.49	15.25	20.66	49.03	32.99	15.78	19.88	49.93	33.09	16.43	19.31
CaO	0.09	0.98	19.47	–	0.06	0.69	21.63	–	0.07	0.91	20.88	–
Na_2O	–	0.14	1.68	–	–	0.06	1.37	–	–	0.11	1.23	–
NiO	0.39	0.12	0.07	0.37	0.29	0.07	0.07	0.31	0.32	0.10	0.07	0.25
Total	100.14	100.30	100.01	100.10	99.96	99.99	100.33	100.60	100.09	100.28	100.41	100.36
Mg#	89.6	90.0	89.6	77.4	90.2	90.6	91.1	75.9	91.3	91.7	91.9	75.1
Cr#		4.3	5.8	10.1		4.8	7.7	15.4		10.7	12.3	25.6
T1	1048				963				1030			
T2	1014				924				1083			

	Harzburgite											
	ML-2				ML-8				ML-9			
mineral	Ol	Opx	Cpx	Sp	Ol	Opx	Cpx	Sp	Ol	Opx	Cpx	Sp
SiO_2	41.62	56.02	53.09	0.07	41.48	56.55	52.86	0.03	41.06	55.97	52.72	0.04
TiO_2	–	0.06	0.10	0.10	–	0.09	0.10	0.07	0.05	–	0.08	0.06
Al_2O_3	0.03	4.01	4.92	45.65	–	2.74	3.41	39.61	–	3.25	3.45	44.05
Cr_2O_3	–	0.62	1.10	23.58	–	0.43	1.08	28.98	0.05	0.44	0.74	24.71
FeO	8.53	5.36	2.60	11.38	9.14	5.77	2.35	14.22	8.83	5.63	2.27	12.63
MnO	0.11	0.10	0.08	0.13	0.10	0.12	0.08	0.13	0.10	0.11	0.07	0.12
MgO	49.14	32.51	16.17	19.20	48.94	33.39	16.24	17.36	49.36	33.46	16.68	18.23
CaO	0.07	0.96	20.96	–	0.03	0.57	23.08	–	0.06	0.65	23.47	–
Na_2O	0.02	0.10	1.26	–	–	0.05	0.80	–	0.02	0.03	0.59	–
NiO	0.42	0.10	0.07	0.28	0.40	0.07	0.04	0.22	0.37	0.09	0.04	0.25
Total	99.94	99.83	100.33	100.39	100.08	99.78	100.05	100.60	99.89	99.61	100.10	100.10
$Mg^{\#}$	91.1	91.5	91.7	75.0	90.5	91.2	92.5	68.5	90.9	91.4	92.9	72.0
$Cr^{\#}$		9.4	13.0	25.7		9.5	17.6	32.9		8.3	12.6	27.3
T1	1042				924				950			
T2	1038				910				937			

	Harzburgite											
	ML-10				ML-11				ML-13			
mineral	Ol	Opx	Cpx	Sp	Ol	Opx	Cpx	Sp	Ol	Opx	Cpx	Sp
SiO_2	41.78	57.80	53.94	0.04	41.43	56.96	53.65	–	41.46	56.51	53.18	0.04
TiO_2	–	–	0.07	0.06	–	0.05	0.09	0.06	0.04	0.06	0.03	0.01
Al_2O_3	–	1.82	2.09	26.18	–	2.13	2.56	37.93	–	2.82	2.61	44.20
Cr_2O_3	–	0.46	1.02	42.55	–	0.37	0.76	30.13	0.02	0.38	0.63	23.88
FeO	8.43	5.28	2.11	15.88	8.71	5.71	2.05	14.59	9.18	5.99	2.20	13.70
MnO	0.12	0.14	0.07	0.14	0.10	0.15	0.10	0.15	0.12	0.11	0.04	0.14
MgO	48.91	33.55	16.92	15.01	49.02	33.66	16.36	16.87	48.78	33.12	16.77	17.86
CaO	0.04	0.65	23.35	–	0.02	0.42	23.76	–	0.03	0.51	24.41	–
Na_2O	–	0.04	0.60	–	–	0.02	0.59	–	–	0.02	0.23	–
NiO	0.38	0.10	0.06	0.15	0.37	0.07	0.05	0.18	0.39	0.08	0.05	0.24
Total	99.66	99.84	100.22	100.01	99.65	99.54	99.97	99.90	100.02	99.60	100.17	100.08
$Mg_{\#}$	91.2	91.9	93.5	62.8	90.9	91.3	93.4	67.3	90.4	90.8	93.1	69.9
$Cr_{\#}$		14.4	24.6	52.2		10.5	16.6	34.8		8.3	13.9	26.6
T1	949					864				901		
T2	883					864				895		

	Harzburgite							
	ML-14				ML-15			
mineral	Ol	Opx	Cpx	Sp	Ol	Opx	Cpx	Sp
SiO_2	41.58	57.37	54.32	0.05	40.90	56.75	53.71	0.04
TiO_2	–	–	0.07	0.09	0.05	0.04	0.05	0.10
Al_2O_3	–	1.96	2.19	28.81	0.03	2.51	2.81	27.75
Cr_2O_3	0.02	0.45	0.87	39.65	0.05	0.59	1.06	41.24
FeO	8.70	5.60	2.13	16.07	8.49	5.27	2.44	14.45
MnO	0.09	0.12	0.07	0.18	0.12	0.12	0.05	0.16
MgO	48.94	33.54	16.77	15.50	49.57	33.16	17.12	16.14
CaO	0.04	0.60	23.28	0.01	0.09	1.00	21.99	–
Na_2O	–	0.04	0.63	–	–	0.07	0.69	–
NiO	0.35	0.07	0.05	0.18	0.36	0.08	0.06	0.18
Total	99.71	99.75	100.38	100.54	99.65	99.60	99.97	100.07

(continued on next page)

Table 2 (*continued*)

	Harzburgite							
	ML-14				ML-15			
mineral	Ol	Opx	Cpx	Sp	Ol	Opx	Cpx	Sp
$Mg^{\#}$	90.9	91.4	93.3	63.2	91.2	91.8	92.6	66.6
$Cr^{\#}$		13.3	21.1	48.0		13.5	20.3	49.9
T1	933				1054			
T2	887				961			

1 Mineral composition is the average of 5 analyses.
2 Mg# = molar 100 Mg/(Mg + Fe), and Cr# = molar 100Cr/(Cr + Al).
3 T1 and T2 are calculated using the Ca-opx thermometer of Brey and Köhler (1990) and Cr-Al-opx thermometer of Witt-Eickschen and Seck (1991), respectively. Pressures of 1.5 GPa are assumed throughout.

4. Results

4.1. Whole rock major element compositions

Whole rock major element abundances are given in Table 1. Al_2O_3, CaO and TiO_2 correlate negatively with MgO (Fig. 4), forming trends similar to the global one defined by mantle xenoliths and massive peridotites (e.g., Takazawa et al., 2000). Consistent with their mineral modal composition, the majority of the Yantai peridotites are refractory harzburgites, with high MgO content (>42 wt.%) and Mg# value (>90.5), low CaO (<2.0 wt.%), Al_2O_3 (<2.0 wt.%) and TiO_2 (<0.04 wt.%) contents. Only three lherzolites (sample ML-3, ML-4 and ML-5) display a relatively fertile composition. In particular, sample ML-5 has a distinctly high CaO content (>5 wt.%; Fig. 4d), due to its anomalously high cpx mode (24%; Table 1). The compositions of sample ML-4 and ML-5 are close to that of the primitive mantle (Hart and Zindler, 1986; Jagoutz et al., 1979).

4.2. Mineral chemistry and equilibrium temperature

Mineral compositions are listed in Table 2. No compositional zonation has been observed in constituent minerals, suggesting a homogeneous composition and chemical equilibrium between minerals.

Ol in the Yantai peridotites shows a wide range of Mg/(Mg + Fe) (Mg#) ratio (89.6 to 91.3). Ol in the lherzolites displays a lower Mg# (89.6–90.2) than in the harzburgites (90.4–91.3). Difference in Mg# is also observed for opx and cpx in the two groups; for instance, $Mg\#_{opx}$ (90.0 to 90.6) in lherzolites is lower than in harzburgites (>90.6). The refractoriness of the harzburgite samples is also reflected by its high $Cr\#_{sp}$ (>20) which is a measure of degree of partial melting. In spite of

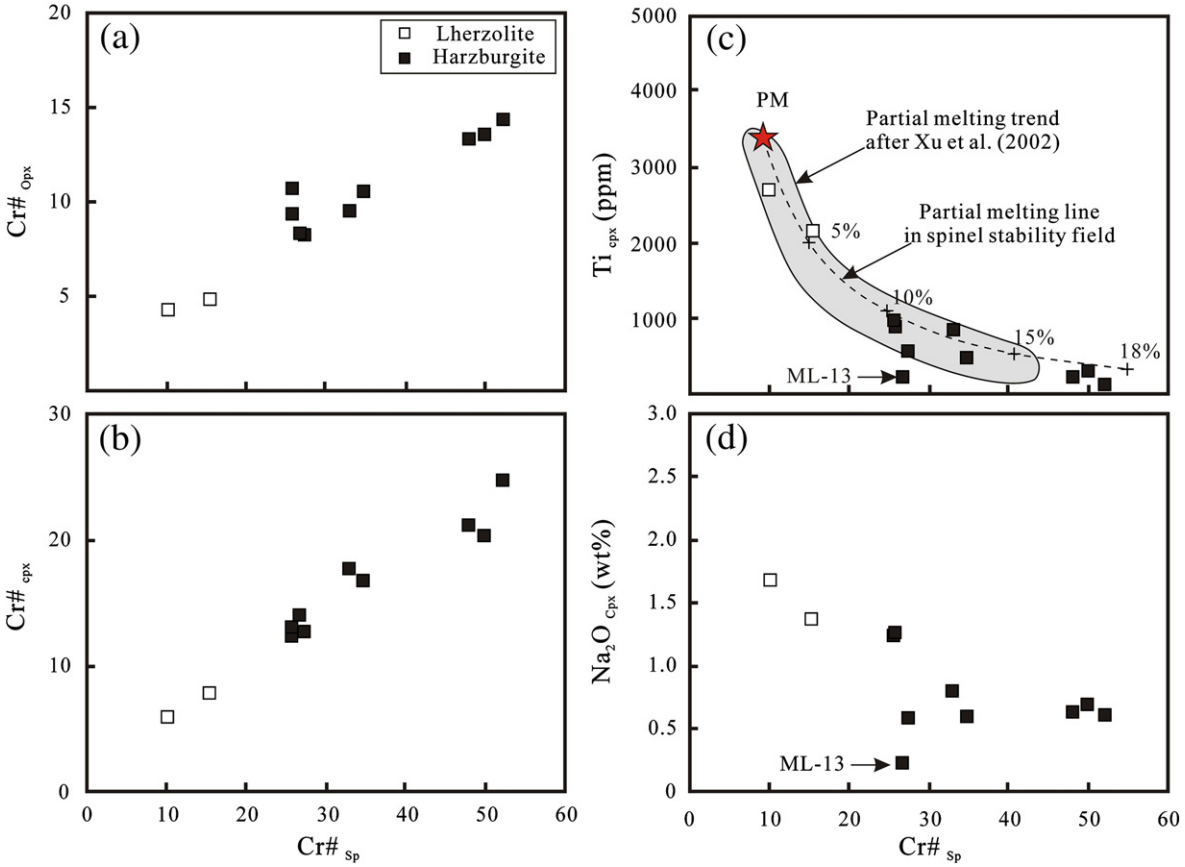

Fig. 5. Plots of (a) $Cr\#_{cpx}$, (b) $Cr\#_{opx}$, (c) Ti content in cpx, and (d) Na_2O in cpx against $Cr\#_{sp}$. The melting trend in (c) is calculated using fractional melting model within spinel stability field (Hellebrand et al., 2001; Johnson et al., 1990). Partition coefficient for Ti between melt and clinopyroxene is from Sobolev et al. (1996). For comparison, the commonly melting trend after Xu et al. (2002) is also shown. The majority of the Yantai samples plot along the common melting trend, but sample ML-13 shows anomalously low Ti content in cpx at given $Cr\#_{sp}$.

predominant refractory harzburgites, the Yantai peridotites dislike the cratonic peridotites (Boyd, 1989). They all fall along the oceanic trend in the plot of ol mode against forsterite content in ol (Fo), typical of the Phanerozoic mantle (Fig. 2c).

The linear correlations between Cr# of spinel ($Cr\#_{sp}$) and Cr# of opx and cpx (Fig. 5a, b) strongly indicate chemical equilibrium between co-existing minerals. Similar to those defined by unmetasomatized peridotites from around the world, Ti and Na_2O contents in cpx progressively decrease with increasing $Cr\#_{sp}$ (Fig. 5c, d). Sample ML-13 deviates from the melting curve due to its low Ti content (246 ppm) but a moderate $Cr\#_{sp}$ (Fig. 5c).

Temperatures were calculated using the Ca-in-opx thermometer (Brey and Köhler, 1990) and the empirical thermometer (Witt-Eickschen and Seck, 1991), based on Cr–Al exchange between opx and sp. For most samples, the two thermometers yield broadly similar estimates of 850–1080 °C (Table 2). This temperature range is relatively larger than those of other peridotite xenoliths from Shandong Peninsula (Penglai: 925–975 °C, Shanwang: 925–975 °C, Qixia: 850–925 °C; recalculated using the data of Chu et al., 2009; Zheng et al., 1998). This suggests that the Yantai samples may come from a relatively large depth interval of the SCLM. The samples with relatively high temperature estimates (sample ML-1, ML-2 and ML-4) are all severely metasomatized by silicate melts (see below).

4.3. Trace element compositions

4.3.1. Whole rock

Three types of REE patterns can be distinguished in the Yantai peridotites (Fig. 6).

(1) Three samples (sample ML-1, ML-2 and ML-5) have essentially flat REE patterns with La/Sm equal to 1 or slightly less than 1 (Fig. 6a). They also exhibit negative anomalies of Ba, Zr and Ti, and enrichment of Nb, Th, U and Rb (Fig. 6b).

(2) Five samples (sample ML-4, ML-8, ML-9, ML-12, and ML-13) show a V-shaped REE pattern, characterized by a fractionated HREE and an enriched LREE distribution [$(La/Sm)_N > 1$] (Fig. 6c). In primitive mantle (PM)-normalized spidergram, a peak at U–Nb and positive anomalies of Sr and Zr are commonly observed (Fig. 6d).

(3) LREE-enriched patterns [$(La/Sm)_N > 1$] are primarily observed in refractory harzburgites (Fig. 6e). HREE contents in the harzburgites with this type of pattern are generally lower than in lherzolites (Table 1), suggesting that metasomatism tend to be associated with refractory samples. In PM-normalized spidergram, a peak at Th–Nb and weak positive anomalies of Sr and Zr, but significant negative anomalies of Ba are found in representative samples. Two samples (sample

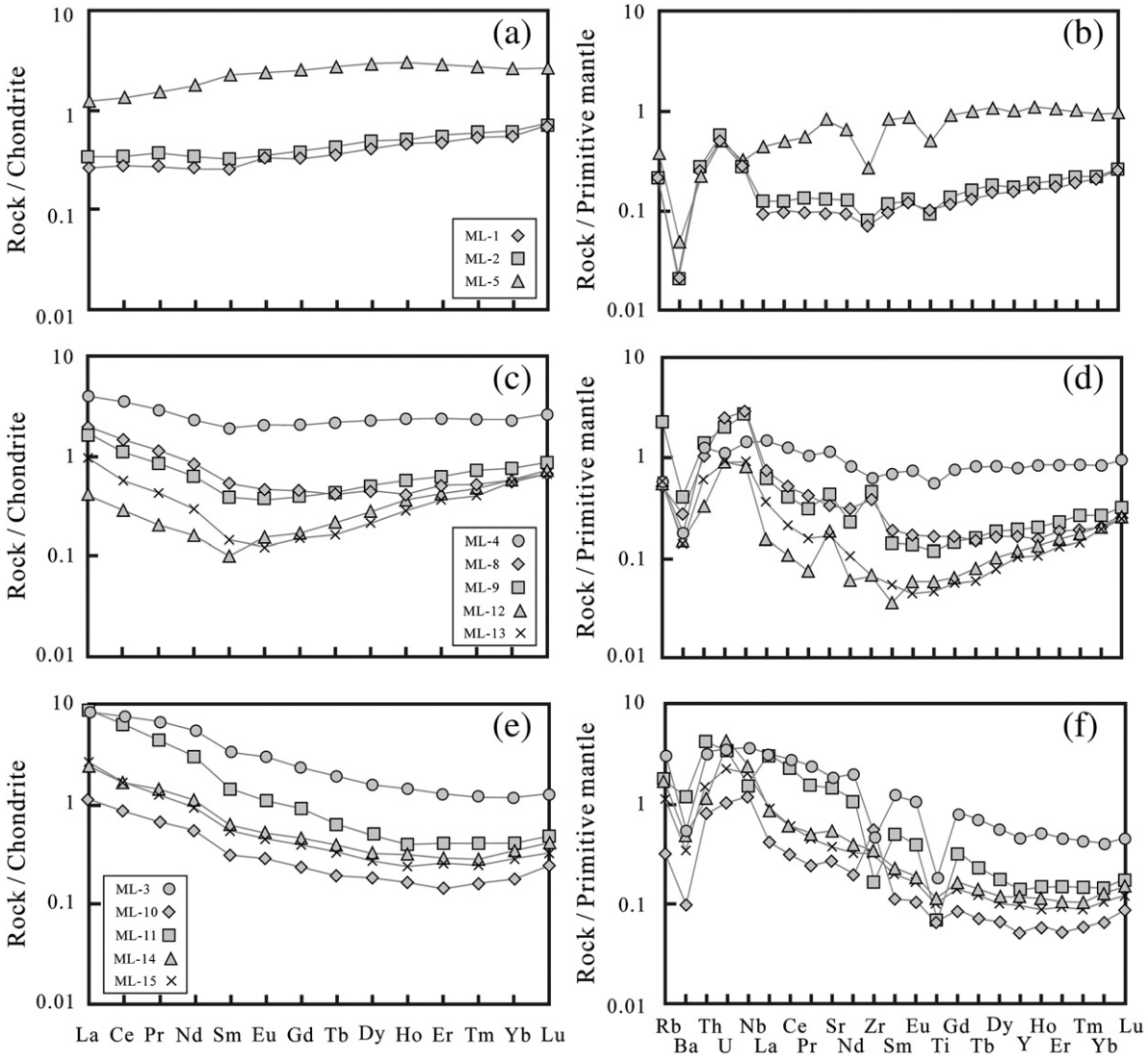

Fig. 6. Whole rock REE and trace element abundances in Yantai peridotites. Normalization values are from McDonough and Sun (1995).

Table 3
Trace element compositions in clinopyroxene (ppm) from Yantai peridotites.

	Lherzolite			Harzburgite									
	ML-3	ML-4	ML-5	ML-1	ML-2	ML-8	ML-9	ML-10	ML-11	ML-12	ML-13	ML-14	ML-15
Sr	226.18	158.39	58.42	36.43	32.40	4.59	1.14	37.94	20.97	2.08	1.77	27.59	80.87
Ti	881	2702	2166	973	895	857	579	133	499	414	236	240	322
Y	9.72	16.00	13.00	9.43	9.11	7.23	6.64	1.90	5.08	5.05	3.32	2.56	3.08
Zr	1.77	30.71	8.81	11.70	10.59	2.93	0.74	6.51	8.23	0.87	0.26	10.17	8.53
Nb	2.18	2.69	0.26	0.82	0.73	0.13	0.07	0.37	0.26	0.26	0.09	0.23	1.03
Ba	0.89	0.14	0.05	0.13	0.18	0.45	0.33	0.11	0.23	0.13	0.14	0.56	0.47
La	8.31	6.33	0.73	1.28	1.16	0.12	0.02	0.61	1.52	0.14	0.22	0.80	4.50
Ce	21.82	13.14	2.01	3.21	2.98	0.37	0.04	1.66	3.67	0.10	0.35	3.32	6.52
Pr	2.71	1.42	0.32	0.46	0.43	0.07	0.01	0.25	0.52	0.01	0.03	0.58	0.50
Nd	12.50	6.53	2.28	2.81	2.64	0.52	0.15	1.39	2.72	0.14	0.12	3.03	1.80
Sm	2.35	1.83	1.11	0.97	0.92	0.29	0.14	0.35	0.63	0.11	–	0.60	0.42
Eu	0.84	0.72	0.47	0.37	0.38	0.14	0.09	0.14	0.22	0.08	0.02	0.19	0.18
Gd	1.98	2.42	1.72	1.36	1.22	0.63	0.48	0.37	0.64	0.31	0.12	0.51	0.49
Tb	0.28	0.42	0.33	0.24	0.22	0.14	0.11	0.05	0.11	0.07	0.04	0.08	0.08
Dy	1.96	3.11	2.39	1.88	1.79	1.24	1.03	0.37	0.90	0.80	0.46	0.51	0.64
Ho	0.37	0.60	0.50	0.37	0.36	0.28	0.24	0.07	0.19	0.19	0.12	0.10	0.12
Er	1.10	1.87	1.47	1.14	1.08	0.93	0.82	0.24	0.67	0.67	0.48	0.32	0.37
Tm	0.14	0.24	0.20	0.13	0.14	0.13	0.12	0.03	0.09	0.09	0.07	0.04	0.05
Yb	1.08	1.82	1.51	1.03	1.02	0.96	0.86	0.28	0.70	0.79	0.60	0.38	0.39
Lu	0.14	0.21	0.19	0.13	0.12	0.13	0.12	0.04	0.09	0.10	0.07	0.05	0.05
$(La/Yb)_N$	5.22	2.37	0.33	0.84	0.77	0.09	0.02	1.47	1.48	0.12	0.25	1.43	7.86
∑REE	55.57	40.65	15.22	15.38	14.43	5.94	4.23	5.87	12.66	3.58	2.97	10.50	16.11
Ti/Eu	1053	3733	4583	2632	2340	6151	6643	982	2318	5462	11735	1237	1824
Ba/La	0.11	0.02	0.07	0.10	0.15	3.65	16.97	0.17	0.15	0.98	0.61	0.70	0.10
Sr/Nd	18	24	26	13	12	9	8	27	8	15	15	9	45

Subscript N in $(La/Yb)_N$ denotes chondrite-normalized.

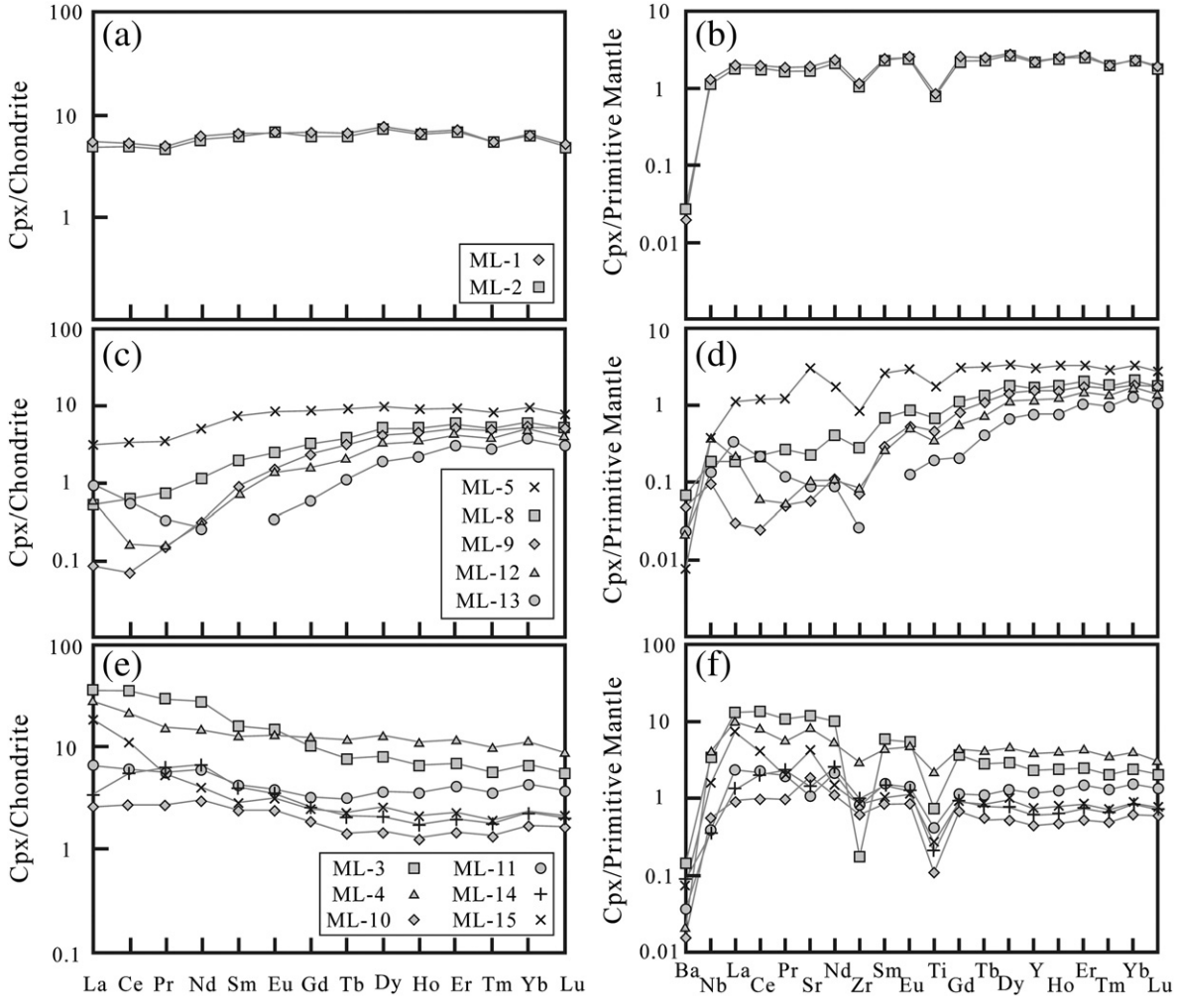

Fig. 7. REE and trace element pattern in clinopyroxene from Yantai peridotites. Normalization values are from McDonough and Sun (1995).

Table 4
Re–Os isotope compositions of Yantai peridotites.

	Re (ppb)	Os (ppb)	$^{187}Re/^{188}Os$	$^{187}Os/^{188}Os$	2σ	T_{RD} (Ma)	T_{MA} (Ma)
ML-1	0.015	1.230	0.060	0.1171	0.0008	1701	1971
ML-2	0.218	0.890	1.180	0.1206	0.0008	1233	−732
ML-3	0.003	4.352	0.003	0.1237	0.0006	813	818
ML-4	0.033	1.506	0.106	0.1244	0.0008	717	944
ML-5	0.104	1.428	0.351	0.1262	0.0007	467	2373
ML-8	0.014	0.116	0.562	0.1193	0.0010	1415	−5097
ML-9	0.018	0.917	0.097	0.1248	0.0006	664	853
ML-10	0.014	1.545	0.044	0.1230	0.0005	909	1010
ML-11	0.685	1.944	1.694	0.1199	0.0007	1335	−468
ML-12	0.121	1.493	0.390	0.1245	0.0008	701	6482
ML-13	0.017	0.521	0.158	0.1253	0.0009	590	923
ML-14	0.011	0.106	0.524	0.1218	0.0013	1072	−5554
ML-15	0.016	2.227	0.034	0.1171	0.0006	1701	1841
ML-15R	0.027	2.128	0.061	0.1179	0.0003	1604	1860

The parameters used in the calculation are $\lambda_{Re} = 1.666 \times 10^{-11}$/year, $(^{187}Re/188Os)_{Chond} = 0.435$ (Bennett et al., 2002) and $(^{187}Os/^{188}Os)_{Chond} = 0.1296$ (Meisel et al., 2001). All Re contents have been corrected for blanks, except sample ML-3, due to its unusually low Re content.

ML-3 and ML-11) distinguish themselves by their significant negative anomalies of Zr and Ti.

4.3.2. Clinopyroxenes

For a given sample, cpx and whole rocks display essentially similar trace element distribution patterns, although the concentration level is higher for cpx (Table 3). This is consistent with the notion that cpx is the main host for incompatible elements in dry spinel peridotites (e.g., Xu et al., 2002). Nevertheless, some difference is observed between whole rock and cpx compositions.

(1) While the flat and LREE-enriched patterns are observed both in whole rock and cpx compositions, the V-shaped REE pattern illustrated by whole rock compositions is not observed in cpx, except one sample (sample ML-13). Instead, a LREE-depleted pattern $[(La/Yb)_N = 0.09–0.33]$ with a flat HREE pattern $[(Ho/Yb)_N = 0.7–1]$ (Fig. 7c) is observed in cpx. Some samples show inflection of La and Ce (Fig. 7c). Combined with the enrichment of Nb (Fig. 7d), the inflection of La and Ce possibly indicates incipient enrichment of highly incompatible elements. Ti, Zr and Hf occur as weak negative spikes in PM-normalized distribution patterns (Fig. 7d).
(2) In the samples with LREE-enriched pattern, sample ML-14 show a concave downward REE pattern (Fig. 7e).

4.4. Re–Os isotopes

Re and Os concentrations of most Yantai peridotites vary from <0.01 ppb to 0.2 ppb, and from ~0.5 ppb to >4 ppb, respectively (Table 4). These Os concentrations are similar to off-cratonic spinel peridotites from around the world (e.g., Meisel et al., 2001; Pearson et al., 2004; Peslier et al., 2000; Wu et al., 2006), but are lower than Os concentrations in peridotite massifs. Most of the Yantai peridotites

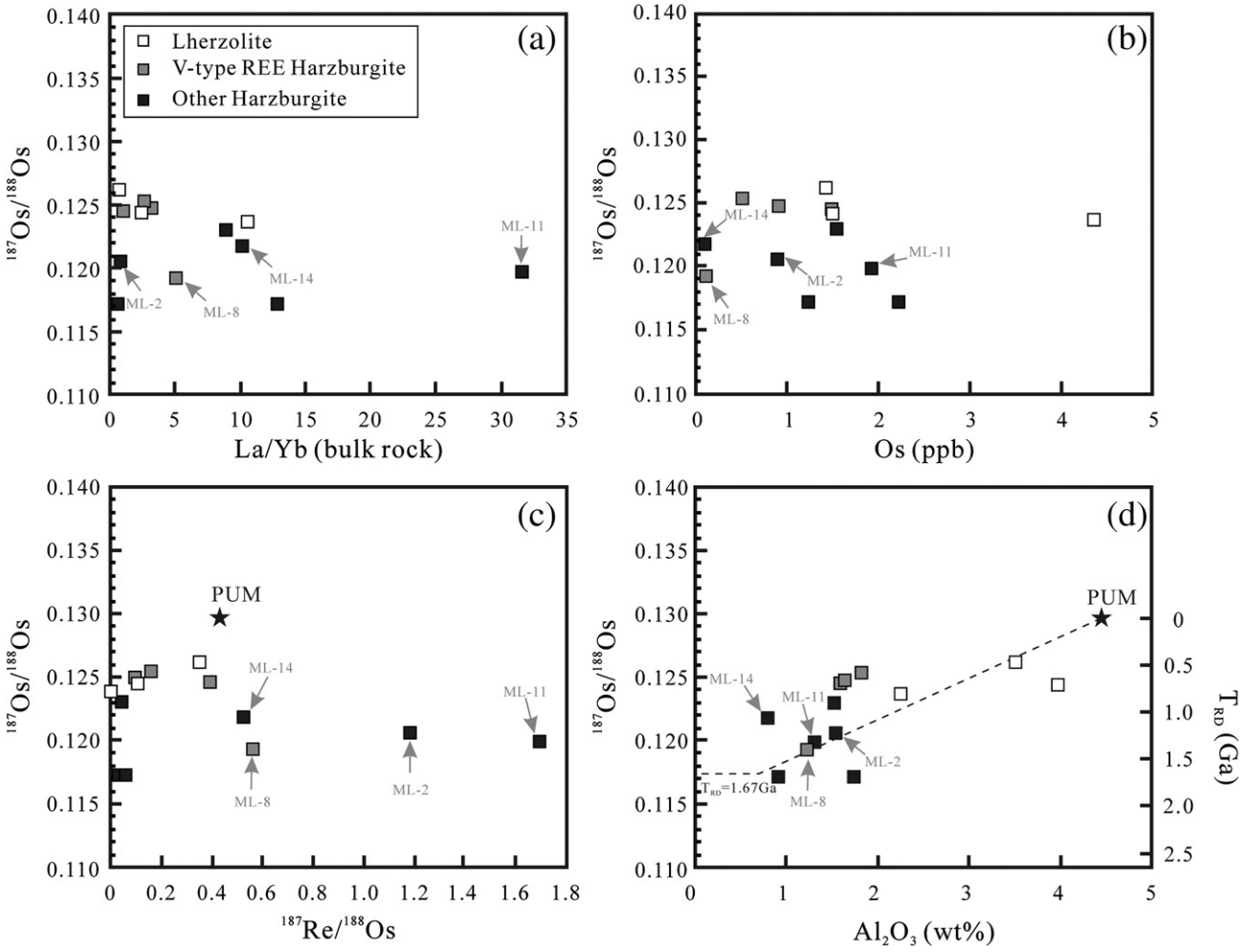

Fig. 8. Whole rock $^{187}Os/^{188}Os$ ratios of Yantai peridotites against (a) La/Yb ratios, (b) Os contents, (c) $^{187}Re/^{188}Os$ ratios and (d) Al_2O_3 (wt%). $^{187}Re/^{188}Os$ ratio, $^{187}Os/^{188}Os$ ratio and Al_2O_3 of the primitive upper mantle (PUM) are from Bennett et al. (2002), Meisel et al. (2001), and McDonough and Sun (1995), respectively.

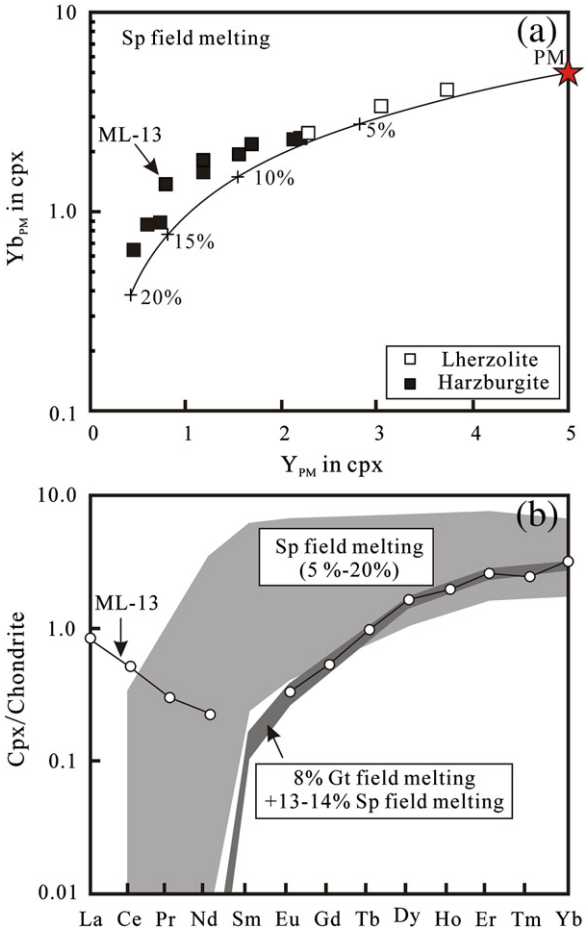

Fig. 9. (a) Comparison of Y and Yb contents of cpx in Yantai peridotites with the calculated melting trend using fractional melting model within spinel stability field (Norman, 1998). Note that the deviation of some harzburgites from the melting trend. The subscript PM indicates that the Y and Yb concentrations are normalized to primitive mantle (McDonough and Sun, 1995). (b) Comparison of REE pattern of Yantai peridotites with the calculated REE pattern of polybaric fractional melting. See text for details. For comparison, the range of the calculated REE pattern of spinel field melting is also shown. Within garnet stability field melting, the starting material compositions and the melt modal compositions are 55%ol + 20%opx + 15%cpx + 10%gt, and 8%ol − 19%opx + 81%cpx + 30%gt (after Walter, 1998), respectively. Within spinel stability field melting, 53%ol + 25%opx + 20%cpx + 2%sp for the starting material compositions, and −6%ol + 28%opx + 67%cpx + 11%sp (after Kinzler, 1997) are used. Decompression reaction of garnet is after Xu et al. (2002): 0.2 ol + gt = 0.5 opx + 0.5 cpx + 0.2 sp. The partition coefficients for REE between melt and minerals are after Johnson (1998).

have $^{187}Re/^{188}Os$ ratios less than 0.4, but four samples have the $^{187}Re/^{188}Os$ ratios greater than 0.5, either due to their high Re contents (>0.2 ppb for sample ML-2 and ML-11), or owing to their low Os contents (<0.2 ppb for sample ML-8 and ML-14).

$^{187}Os/^{188}Os$ ratios range from 0.1171 to 0.1263, similar to those reported for other peridotite xenoliths from Shandong Peninsula (Chu et al., 2009; Gao et al., 2002). All the ratios are lower than that of the present-day primitive upper mantle (PUM) value (0.129 ± 1; Meisel et al., 2001). Among these, five samples (sample ML-1, ML-2, ML-8, ML-11 and ML-15) have the $^{187}Os/^{188}Os$ ratios less than 0.121. Using the parameter of $(^{187}Os/^{188}Os)_{Chond} = 0.1296$ (Meisel et al., 2001), the calculated T_{RD} ages are older than 1.2 Ga.

No clear correlation is observed between $^{187}Os/^{188}Os$ ratio and La/Yb ratio (and Os contents) for the whole suite (Fig. 8a, b). Similar to peridotite xenoliths from other places, the relationship between $^{187}Os/^{188}Os$ and $^{187}Re/^{188}Os$ of the Yantai peridotites is very poor (Fig. 8c), probably due to the disturbance of Re–Os isotopic system in post-melting processes. There is a weak positive correlation between $^{187}Os/^{188}Os$ and Al_2O_3 in Yantai peridotites for the whole suite (Fig. 8d).

5. Discussions

5.1. Mantle depletion

5.1.1. Yantai peridotites as residues of partial melting

The Yantai peridotites range from cpx-rich lherzolites (cpx > 10%) via cpx-poor lherzolites to harzburgites (cpx <5%) (Table 1; Fig. 2a). Such a modal variation is accompanied by whole rock and mineral composition changes (Figs. 4 and 5). In particular, the inverse correlations between CaO (TiO_2 and Al_2O_3) and MgO are similar to those observed for residual peridotites from worldwide occurrences (Fig. 4; e.g., Takazawa et al., 2000). The melt depletion is also evidenced from mineral compositions, which show decreasing Ti and Na_2O in cpx with increasing $Cr\#_{sp}$ (Fig. 5c, d). These compositional variations are similar to those defined by unmetasomatized peridotites from around the world, suggesting the primary control of partial melting on mineral compositions (e.g., Yaxley et al., 1998). We thus conclude that the Yantai peridotites represent the residues left after extracting basalts by variable degrees of partial melting.

5.1.2. Evidence for melting in garnet stability field

Fig. 9a compares Y and Yb in cpx from the Yantai peridotites with modeled curve of fractional melting of the spinel peridotites. The Yantai lherzolites fall along the partial melting line, constraining the degree of partial melting less than 10%. However, most harzburgites deviate from the line (Fig. 9a) due to their higher Yb at a given Y content, suggesting a fractionation between these two elements. Because of their essentially similar partition coefficients between cpx and melt (e.g., Johnson, 1998), Y and Yb would not fractionate from each other in the spinel stability field, even during high degrees of partial melting. Such a fractionation cannot be related to mantle metasomatism either, because Y is slightly more incompatible than Yb in basaltic system (Sun and McDonough, 1989) and metasomatism would result in enrichment of Y over Yb, placing the samples below the modeled melting trend in Fig. 9a. In fact, both Y and Yb form negative correlations with MgO (Fig. 4g and h), suggesting that they were not affected by metasomatism.

The fractionation between Y and Yb may be indicative of the involvement of garnet during mantle melting, because HREE and Y in garnet are highly fractionated (e.g., Johnson, 1998). Because the HREE-fractionated cpx is observed in spinel facies peridotites, it requires the breakdown of former garnet and final re-equilibration in the spinel stability field. We thus propose that some Yantai peridotites are residues of melting of garnet peridotites with variable amounts of garnet that has subsequently broken down to cpx. Similar petrogenetic models have been proposed for the peridotite xenoliths from Samoan (Hauri and Hart, 1994), Qilin (Xu et al., 2002) and other places (Hellebrand et al., 2002; Johnson et al., 1990). This petrogenetic model gains its supporting evidence from clusters of spinels with holly-leaf shape and pyroxenes in the Yantai peridotites (Fig. 3b), which is commonly interpreted as a result of breakdown of former garnet (Nicolas, 1986).

In order to test this model, we performed a calculation using the fractional melting model of Johnson et al. (1990) to monitor the REE variation during polybaric melting, which starts in the stability field of garnet lherzolite, followed by the breaking down of garnet into cpx and opx and then by the continuing melting in the spinel stability field (see caption of Fig. 9b for the parameters used in modeling). The amount of melting in the garnet field is adjusted to simulate the observed degree of HREE fractionation in cpx, whereas the absolute concentration of the HREE is sensitive to the degree of the melting in the spinel field. Fig. 9b compares the modeling results with the REE pattern of cpx in the Yantai peridotites. The cpx composition of sample ML-13 can be nicely fitted by 8% melting in stability field of garnet lherzolite firstly, and then continued to melt 13–14% degree in spinel stability field after garnet breakdown. The total degree of melting

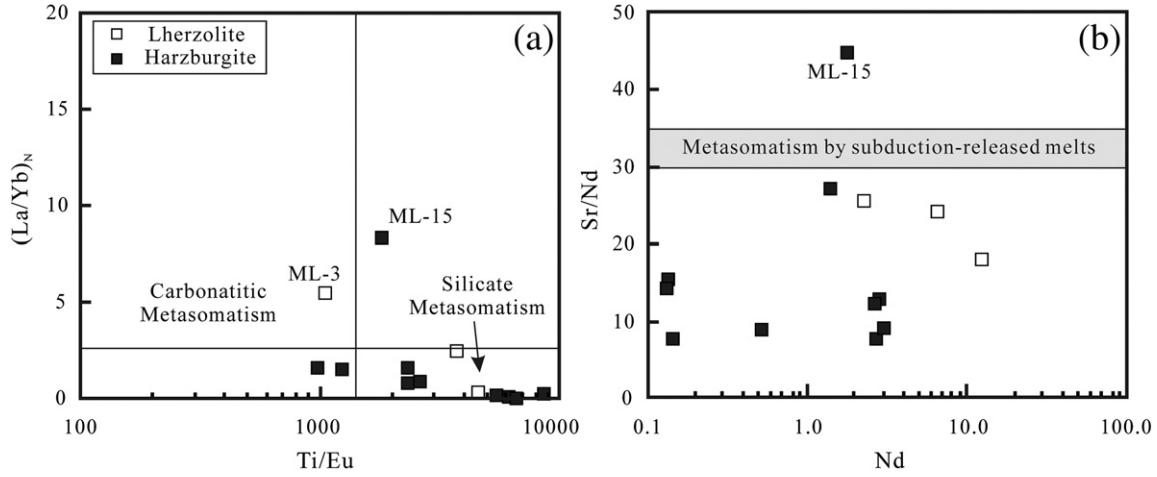

Fig. 10. (a) Ti/Eu ratio vs $(La/Yb)_N$ ratio in clinopyroxene from Yantai peridotites. Fields of carbonate and silicate metasomatism are after Coltorti et al. (1999). (b) Nd contents (ppm) vs Sr/Nd ratios in clinopyroxene from Yantai peridotites. The grey area denotes metasomatism by subduction-released melts (after McDonough, 1990).

amounts to 21–22%. Such high degree of partial melting of spinel lherzolite would have exhausted all the cpx in the residual source (Walter, 2003; and references therein), which is not the case of sample ML-13 (~6% cpx; Table 1). A reasonable explanation is the generation of excess cpx during the breakdown of garnet. The polybaric melting also explains the deviation of sample ML-13 from the melting curve in Fig. 5c. The deviation is owing to its very low Ti content in cpx (236 ppm) and moderate $Cr\#_{sp}$, which partly inherits the low Cr# of garnet (Xu et al., 2002).

Whether characteristics pertinent to polybaric melting (highly fractionated HREE, low Ti at moderate Cr#sp, anomalously high cpx mode) are visible depends on the content of former garnet in the mantle and the melting extent within garnet stability field. As shown by Xu et al. (2002), the visible HREE fractionation requires relatively extensive partial melting (>20%) and melting in the garnet field not less than 8%. Modeling shows that for most Yantai samples experienced <8% melting in the garnet field, therefore accounting for the scarcity of visible HREE fractionation in the spinel peridotites.

5.2. Mantle enrichment

5.2.1. Evidence for metasomatic enrichment

The majority of the Yantai samples show sign of metasomatic enrichment in highly incompatible elements (Fig. 4e and f). Chromatographic-type migration of LREE-enriched melts/fluids through LREE-depleted peridotites (Bodinier et al., 1990; Navon and Stolper, 1987) may be a viable mechanism to produce variable LREE enrichments observed in the Yantai peridotites. This is because during chromatographic metasomatism, elements move through the porous peridotites at rates inversely proportional to their solid-melt partition coefficients. The enrichment front of the most incompatible elements moves faster than that of less incompatible elements.

The metasomatic enrichment in the Yantai peridotites is characterized by high Nb abundance, low Ba/La and Sr/Nd and relatively high Ti/Eu (Table 3; Fig. 10). Neither hydrous fluids nor carbonate melts can be the metasomatic agent, because Nb is immobile in hydrous fluids (e.g., Keppler, 1996). Moreover, metasomatism involving carbonate

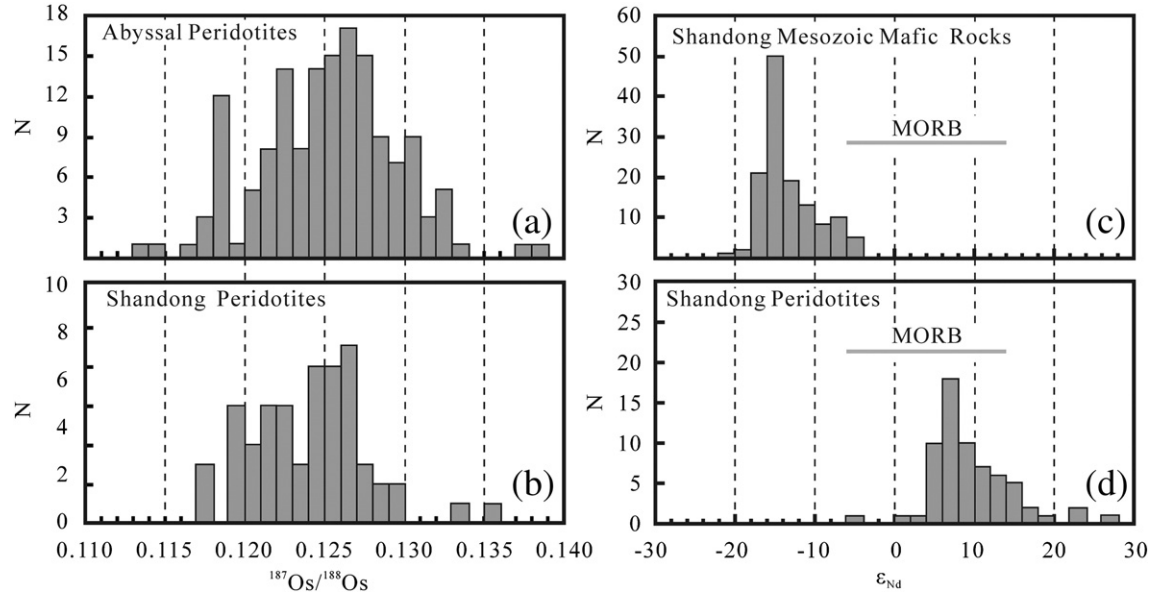

Fig. 11. (a) and (b) Comparison of $^{187}Os/^{188}Os$ of the Yantai peridotite with other xenoliths from Shandong Peninsula and abyssal peridotites. (c) and (d) Comparison of $\varepsilon_{(Nd)}$ of the Mesozoic and Cenozoic lithospheric mantle beneath Shandong Peninsula. The range of $\varepsilon_{(Nd)}$ for MORB is from Hofmann (2003). Data source for Os isotope composition: Shandong peridotites — Chu et al. (2009), Gao et al. (2002); abyssal peridotites — Alard et al. (2005), Brandon et al.(2000), Harvey et al. (2006), Liu et al. (2008a), Martin (1991), Roy-Barman and Allègre (1994), Snow and Reisberg (1995) and Standish et al. (2002). Data source for $\varepsilon_{(Nd)}$ value: Mesozoic rocks in Shandong — Fan et al. (2001), Guo et al. (2001, 2003), Liu et al. (2006, 2008b, 2009), Xu et al. (2004b, c), Yang et al. (2004), Yang et al. (2008), Zhang et al. (2002); Shandong Peninsula peridotites — Chu et al. (2009) and Fan et al. (2000).

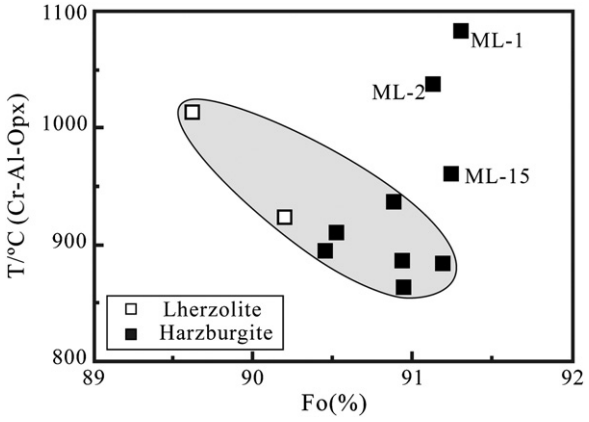

Fig. 12. Plot of equilibrium temperatures against Fo of Yantai peridotites. Equilibrium temperatures are Cr-Al-opx thermometer of Witt-Eickschen and Seck (1991).

melts will yield low Ti/Eu ratio and high $(La/Yb)_N$ ratio (Coltorti et al., 1999), and high CaO content at a given MgO content (Yaxley et al., 1998), which are not observed in the Yantai case (Figs. 4d, 10a). The role of subduction-released melts can also be precluded, because Sr/Nd ratios (<26) in the Yantai peridotites are significantly lower than that of the typical peridotites metasomatized by subduction-released melts (30–35; Fig. 10b). We thus suggest that the metasomatism in these samples was probably related to melts produced by small degree of partial melting of asthenospheric source.

5.2.2. Effect of metasomatism on Re–Os system

Because of the extremely high partition coefficients of Os in sulfides, addition of metasomatic sulfides to mantle residues is an effective way to disturb both Os abundances and Os isotopic ratios of the host peridotites. Alard et al. (2002) reported two types of sulfides in peridotite xenoliths: the "original" type was included in silicate phases, and the secondary type was interstitial along silicate boundaries. The whole rock analyses integrate these different generations of sulfides.

$^{187}Re/^{188}Os$ ratios of four samples (sample ML-2, ML-8, ML-11, ML-14) are higher than that of the PUM (Fig. 8c), suggesting introduction of Re during melt percolation. However, these samples do not display corresponding high $^{187}Os/^{188}Os$ ratios (Fig. 8a). Therefore melt percolation must be recent, otherwise high $^{187}Os/^{188}Os$ would have developed as a result of radiogenic growth subsequent to metasomatic enrichment of Re/Os. These samples (except for sample ML-14) and other samples loosely define a positive correlation between $^{187}Os/^{188}Os$ and Al_2O_3 that extends to the PUM (Fig. 8d), suggesting that not all metasomatism can affect Os isotopes of the mantle. Such a decoupling between enrichment of lithosphile and siderophile elements may be due to the relatively high proportion between primary sulfides and metasomatic sulfides in these samples.

Sample ML-14 plots above the correlation line in Fig. 8d. This sample has very low Os abundance (~0.1 ppb), making it more susceptible to metasomatic Os addition. Hence, a possible explanation is that the relatively high $^{187}Os/^{188}Os$ ratio in sample ML-14 at given Al_2O_3 could have developed as a result of addition of a radiogenic Os component to the peridotites. The other moderately refractory samples (sample ML-9, ML-12, ML-13) also plot above the correlation line in Fig. 8d. The low La/Yb and Re/Os ratios in these samples point to an unaffected Os isotopic composition.

5.3. Age of the lithospheric mantle beneath Shandong Peninsula

T_{RD} model ages, which are calculated by assuming that melting removes all of the Re from the peridotites, yield robust estimates of the minimum age of melt depletion (Walker et al., 1989). Because Re is almost completely removed from the residue at very high degrees of melting, only the Re-depletion age of the most refractory samples may approach that of the true age. In this regard, the two most refractory samples (sample ML-14, ML-15; Al_2O_3<1 wt.%) of the Yantai peridotites may yield meaningful age estimates. As discussed previously, the Os isotopic composition of sample ML-14 may have been affected by metasomatism. It follows that 1.7 Ga for sample ML-15 may represent the minimum age of melt extraction. A Proterozoic age for the SCLM beneath Yantai is also evidenced from the $^{187}Os/^{188}Os$-Al_2O_3 correlation (Reisberg and Lorand, 1995). Four refractory samples loosely define a positive correlation (dashed line) in Fig. 8d. Regression of these data through the PUM composition yields an $^{187}Os/^{188}Os$ ratio of ~0.1174 at Al_2O_3 of 0.7 wt%, corresponding to a depletion age of ~1.67 Ga. Two more fertile samples (sample ML-3 and ML-5) plot along the correlation, suggesting that they may be formed at the same time.

Another five samples plot above the correlation due to their relatively higher $^{187}Os/^{188}Os$ at given Al_2O_3 contents (Fig. 8d). Their model T_{RD} and T_{MA} ages are less than 1.0 Ga (Table 4). It is hard to assess when they formed, because Os model age determinations for peridotites with melt depletion ages less than about 1.0 Ga are very poorly constrained (Wu et al., 2006). Because abyssal peridotites are the fragments of Phanerozoic oceanic lithosphere separating from the Phanerozoic convecting mantle (Brandon et al., 2000; Snow and Reisberg, 1995), their $^{187}Os/^{188}Os$ ratios can therefore be considered representative of the Phanerozoic convecting mantle. Given their Os isotopic similarity to typical abyssal peridotites ($^{187}Os/^{188}Os$>~0.121), these five Yantai samples were likely formed during the Phanerozoic.

The Os isotopic data therefore suggest that both Paleoproterozoic and Phanerozoic SCLM may coexist beneath Shandong Peninsula. This inference is, however, at odds with the relationship between mineral and modal compositions, which indicates an affinity of the Phanerozoic mantle for the Yantai samples (Fig. 2c). This is reminiscent of the debate about the age of the SCLM beneath Shandong. While some believe that the SCLM beneath this region is mostly of Proterozoic in age, representing the relicts of ancient upper mantle which survived the thermo-tectonic destruction of the NCC (e.g., Xiao et al., 2010; Zheng, 2009), others deem that all the SCLM beneath this region was formed during Phanerozoic (Chu et al., 2009; Gao et al., 2002). Although the consistency between the age inferred from the plot of Fo vs olivine mode and that deduced from Os isotopes are not demonstrated yet, we prefer to the idea that the SCLM beneath Shandong is made of Phanerozoic mantle, given the following considerations.

(a) The Os isotopic composition of the abyssal peridotites is an important reference for the interpretation of the Os isotopic data of given peridotites. Although abyssal peridotites are formed during Phanerozoic, their $^{187}Os/^{188}Os$ ratios can be as low as 0.113 (Liu et al., 2008a, 2008b), corresponding to a Paleoproterozoic T_{RD} model age. Such Os model ages may be due to long-time survival of ancient Os isotopic signals in asthenospheric mantle (e.g., Liu et al., 2008a, 2008b). The Shandong peridotites display a range in $^{187}Os/^{188}Os$, virtually similar to that of abyssal peridotites (Fig. 11a and b). If the compositional range of the abyssal peridotites reflects that of convective asthenosphere, this suggests a Phanerozoic age for the SCLM beneath Shandong. In other words, the lithospheric mantle beneath eastern Shandong is newly accreted mantle, conversed from upwelling asthenosphere. Its Os isotopic heterogeneity just inherits that of the convective asthenosphere.

(b) As suggested by geochemistry of mafic rocks, the Mesozoic SCLM in Shandong is characterized by enriched Nd isotopes ($\varepsilon_{Nd(t)} = -6$ to -18; Fig. 11c). In contrast, the Cenozoic lithospheric mantle is depleted in Nd isotopes ($\varepsilon_{Nd(t)} = 0$ to $+28$; Fig. 11d), as indicated by peridotite xenoliths in Cenozoic

basalts. Such a contrast in the composition of Mesozoic and Cenozoic SCLM requires the replacement of ancient and enriched lithospheric mantle by young and depleted mantle (Menzies et al., 1993; Xu, 2001), which must have taken place during the late Mesozoic and early Cenozoic (Xu et al., 2009).

(c) The polybaric melting experienced by the Yantai peridotites implies a decompressional melting, probably as a result of asthenospheric upwelling. If the upwelled asthenosphere (residual upper mantle left by polybaric melting) is converted to the lithosphere, it will retain an inverse correlation between degree of depletion and depth (e.g., Xu et al., 2002), because the degree of partial melting increases from deep to shallow level during the polybaric melting (McKenzie and O'Nions, 1991). This prediction is confirmed by the roughly negative correlation between Fo (as an indicator of depletion) and the equilibrium temperature of peridotites (presumably equivalent to the depth) for the Yantai samples (Fig. 12). Three samples (sample ML-1, ML-2 and ML-15) which deviate from this correlation show the highest estimated temperatures and highest Fo (Fig. 12). The cause of this deviation requires further investigation, but could be related to heating of the lithospheric bottom by underlying asthenosphere.

5.4. Spatial heterogeneity of the SCLM beneath Shandong Peninsula

Spatial heterogeneity of the SCLM beneath Shandong Peninsula has long been recognized, with fertile peridotites beneath the Tanlu fault in contrast with refractory peridotites in the region away from the fault (e.g., Xiao et al., 2010; Zheng et al., 1998). The predominance of refractory harzburgites in the Yantai xenoliths is consistent with this generalization. However, the cause of this lateral heterogeneity of the SCLM remains a matter of debate. Zheng et al. (1998) suggested a complete replacement of the ancient mantle by asthenosphere near the Tanlu fault region, where is the locus of asthenospheric ascent. They argued for a partial replacement in the region away from the Tanlu fault, resulting in the coexistence of old and new mantle in that area. The interpretation presented in this paper, however, suggests that all the SCLM beneath Shandong is newly accreted. In combination with literature data (Chu et al., 2009; Rudnick et al., 2004; Xiao et al., 2010; Zheng et al., 1998), we suggest here that the spatial heterogeneity of the SCLM is created after the replacement of the ancient mantle by upwelling asthenosphere. Fertile composition of the lithosphere mantle beneath the Tanlu fault is partly due to modification of lherzolites by asthenospheric melt (e.g., Xiao et al., 2010). Perhaps the translithospheric Tanlu fault facilitated the ascent and migration of asthenospheric melt and enhanced lithospheric mantle-asthenospheric melt reaction (Menzies et al., 2007; Xiao et al., 2010).

6. Conclusions

(1) The peridotite xenoliths from Yantai (Shandong province) range from relatively fertile lherzolites via cpx-poor lherzolite to refractory harzburgites. The proportion of refractory samples among xenolith population is significantly higher than that beneath the Tanlu fault zone, outlining the spatial heterogeneity of the SCLM beneath Shandong province.

(2) Some of the Yantai peridotites show variable enrichment in LILE, recording the multiple metasomatic enrichments of the SCLM involving small melt fractions derived from the asthenosphere. Nevertheless, their HREE and Y contents are unaffected by post-melting metasomatism and point to a polybaric melting that started in garnet stability field then continued in spinel stability field after breakdown of garnet to pyroxenes and spinel. Such a polybaric melting due to adiabatic decompression of upwelling mantle creates a residual mantle in which degree of depletion decreases with depth.

(3) The Yantai peridotites show a wide range in $^{187}Os/^{188}Os$ ratio (0.117–0.126), corresponding to Proterozoic to Phanerozoic Re-depletion model ages. Unlike this conventional interpretation for a co-existence of Proterozoic and Phanerozoic mantle beneath the studied area, we suggest that the SCLM beneath Yantai is all made of Phanerozoic mantle, because of the similarity of Os isotopic composition between the studied samples and abyssal peridotites. Such an interpretation gains its supports from the oceanic mantle affinity of the Yantai peridotites, and the contrasting Nd isotopic signature between Mesozoic and Cenozoic SCLM beneath this region.

Acknowledgements

The authors thank Y Liu, LL Chen, GQ Hu and X.L. Tu for technical assistance with XRF, EPMA and ICP-MS analyses. Thoughtful and thorough reviews by Dr. C-Z Liu and Dr. K Suzuki are gratefully appreciated. Their suggestions greatly improve this paper. The authors gratefully acknowledge the financial support from the National Science Foundation of China (70914001; 91014007) and the CAS/SAFEA International Partnership Program for Creative Research Teams (KZCX2-YW-Q04-06). This GIGCAS publication no 1557.

References

Alard, O., Griffin, W.L., Pearson, N.J., Lorand, J.P., O'Reilly, S.Y., 2002. New insights into the Re–Os systematics of sub-continental lithospheric mantle from in-situ analysis of sulphides. Earth and Planetary Science Letters 203, 651–663.

Alard, O., Luguet, A., Pearson, N.J., Griffin, W.L., Lorand, J.P., Gannoun, A., Burton, K.W., O'Reilly, S.Y., 2005. In situ Os isotopes in abyssal peridotites bridge the isotopic gap between MORBs and their source mantle. Nature 436, 1005–1009.

Bennett, V.C., Nutman, A.P., Esat, T., 2002. Constraints on mantle evolution from $^{187}Os/^{188}Os$ isotopic compositions of Archean ultramafic rocks from southern West Greenland (3.8 Ga) and Western Australia (3.46 Ga). Geochimica et Cosmochimica Acta 66, 2615–2630.

Bodinier, J.L., Vasseur, G., Vernieres, J., Dupuy, C., Fabries, J., 1990. Mechanisms of mantle metasomatism: geochemical evidence from the Lherz orogenic peridotite. Journal of Petrology 31, 597–628.

Boyd, F.R., 1989. Compositional distinction between oceanic and cratonic lithosphere. Earth and Planetary Science Letters 96, 15–26.

Brandon, A.D., Snow, J.E., Walker, R.J., Morgan, J.W., Mock, T.D., 2000. $^{190}Pt–^{186}Os$ and $^{187}Re–^{187}Os$ systematics of abyssal peridotites. Earth and Planetary Science Letters 177, 319–335.

Brey, G.P., Köhler, T., 1990. Geothermobarometry in four-phase lherzolites II. New thermobarometers, and practical assessment of existing thermobarometers. Journal of Petrology 31, 1353–1378.

Chen, L., 2010. Concordant structural variations from the surface to the base of the upper mantle in the North China Craton and its tectonic implications. Lithos 120, 96–115.

Chu, Z.Y., Wu, F.Y., Walker, R.J., Rudnick, R.L., Pitcher, L., Puchtel, I.S., Yang, Y.H., Wilde, S.A., 2009. Temporal evolution of the lithospheric mantle beneath the Eastern North China Craton. Journal of Petrology 50, 1857–1898.

Coltorti, M., Bonadiman, C., Hinton, R.W., Siena, F., Upton, B.G.J., 1999. Carbonatite metasomatism of the oceanic upper mantle: evidence from clinopyroxenes and glasses in ultramafic xenoliths of Grande Comore, Indian Ocean. Journal of Petrology 40, 133–165.

Fan, W.M., Zhang, H.F., Baker, J., Jarvis, K.E., Mason, P.R.D., Menzies, M.A., 2000. On and off the North China Craton: where is the Archaean keel? Journal of Petrology 41, 933–950.

Fan, W.M., Guo, F., Wang, Y.J., Liu, G., Zhang, M., 2001. Post-orogenic bimodal volcanism along the Sulu orogenic belt in Eastern China. Physics and Chemistry of the Earth, Part A: Solid Earth and Geodesy 26, 733–746.

Gao, S., Rudnick, R.L., Carlson, R.W., McDonough, W.F., Liu, Y.S., 2002. Re–Os evidence for replacement of ancient mantle lithosphere beneath the North China Craton. Earth and Planetary Science Letters 198, 307–322.

Goto, A., Tatsumi, Y., 1996. Quantitative analysis of rock samples by an X-ray fluorescence spectrometer (II). The Rigaku Journal 13, 20–39.

Griffin, W.L., Zhang, A.D., O'Reilly, S.Y., Ryan, G., 1998. Phanerozoic evolution of the lithosphere beneath the Sino-Korean Craton. In: Flower, M.F.J., Chung, S.L., Lo, C.H., Lee, T.Y. (Eds.), Mantle dynamics and plate interactions in East Asia: American Geophysical Union, 27, pp. 107–126.

Guo, F., Fan, W.M., Wang, Y.J., Lin, G., 2001. Late Mesozoic mafic intrusive complexes in North China Block: constraints on the nature of subcontinental lithospheric mantle. Physics and Chemistry of the Earth, Part A: Solid Earth and Geodesy 26, 759–771.

Guo, F., Fan, W.M., Wang, Y.J., Lin, G., 2003. Geochemistry of late Mesozoic mafic magmatism in west Shandong Province, eastern China: characterizing the lost lithospheric mantle beneath the North China Block. Geochemical Journal 37, 63–77.

Hart, S.R., Zindler, A., 1986. In search of a bulk-Earth composition. Chemical Geology 57, 247–267.
Harvey, J., Gannoun, A., Burton, K.W., Rogers, N.W., Alard, O., Parkinson, I.J., 2006. Ancient melt extraction from the oceanic upper mantle revealed by Re–Os isotopes in abyssal peridotites from the Mid-Atlantic ridge. Earth and Planetary Science Letters 244, 606–621.
Hauri, E.H., Hart, S.R., 1994. Constraints on melt migration from mantle plumes: a trace element study of peridotite xenoliths from Savai'i, Western Samoa. Journal of Geophysical Research 99, 24301–24321.
Hellebrand, E., Snow, J.E., Dick, H.J.B., Hofmann, A.W., 2001. Coupled major and trace elements as indicators of the extent of melting in mid-ocean-ridge peridotites. Nature 410, 677–681.
Hellebrand, E., Snow, J.E., Hoppe, P., Hofmann, A.W., 2002. Garnet-field melting and late-stage refertilization in "residual" abyssal peridotites from the Central Indian Ridge. Journal of Petrology 43, 2305–2338.
Hofmann, A.W., 2003. Sampling Mantle Heterogeneity through Oceanic Basalts: Isotopes and Trace Elements. In: Holland, H.D., Turekian, K.K. (Eds.), Treatise on Geochemistry: The Mantle and Core, 2. Elsevier-Pergamon, pp. 1–44.
Jagoutz, E., Palme, H., Baddenhausen, H., Blum, K., Cendales, M., Dreibus, G., Spettel, B., Lorenz, V., Waenke, H., 1979. The abundances of major, minor and trace elements in the Earth's mantle as derived from primitive ultramafic nodules. Proceedings of the Lunar and Planetary Science Conference 10th, 2, pp. 2031–2050.
Johnson, K.T.M., 1998. Experimental determination of partition coefficients for rare earth and high-field-strength elements between clinopyroxene, garnet and basaltic melt at high pressures. Contributions to Mineralogy and Petrology 133, 60–68.
Johnson, K.T.M., Dick, H.J.B., Shimizu, N., 1990. Melting in the oceanic upper mantle: an ion microprobe study of diopsides in abyssal peridotites. Journal of Geophysical Research 95, 2661–2678.
Keppler, H., 1996. Constraints from partitioning experiments on the composition of subduction-zone fluids. Nature 380, 237–240.
Kinzler, R.J., 1997. Melting of mantle peridotite at pressures approaching the spinel to garnet transition: application to mid-ocean ridge basalt petrogenesis. Journal of Geophysical Research 102, 853–874.
Li, J., Zhong, L.F., Tu, X.L., Hu, G.Q., Sun, Y.M., Liang, X.R., Xu, J.F., 2011. Platinum group elements and Re–Os isotope analyses for geological samples using a single digestion procedure. Geochimica 40, 1–9 (In Chinese with English Abstract).
Liu, D.Y., Nutman, A.P., Compston, W., Wu, J.S., Shen, Q.H., 1992. Remnants of ≥3800 crust in the Chinese part of the Sino-Korean craton. Geology 20, 339–342.
Liu, Y., Liu, H.C., Li, X.H., 1996. Simultaneous and precise determination of 40 trace elements in rock samples using ICP-MS. Geochimica 25, 552–558 (In Chinese with English Abstract).
Liu, S., Zou, H.B., Hu, R.Z., Zhao, J.H., Feng, C.X., 2006. Mesozoic mafic dikes from the Shandong Peninsula, North China Craton: petrogenesis and tectonic implications. Geochemical Journal 40, 181–195.
Liu, C.Z., Snow, J.E., Hellebrand, E., Brügmann, G., Handt, A.V., Büchl, A., Hofmann, A.W., 2008a. Ancient, highly heterogeneous mantle beneath Gakkel ridge, Arctic Ocean. Nature 452, 311–316.
Liu, S., Hu, R.Z., Gao, S., Feng, C.X., Qi, L., Zhong, H., Xiao, T.F., Qi, Y.Q., Wang, T., Coulson, I.M., 2008b. Zircon U–Pb geochronology and major, trace elemental and Sr–Nd–Pb isotopic geochemistry of mafic dykes in western Shandong Province, east China: constrains on their petrogenesis and geodynamic significance. Chemical Geology 255, 329–345.
Liu, S., Hu, R.H., Gao, S., Feng, C.X., Yu, B.B., Feng, G.Y., Qi, Y.Q., Wang, T., Coulson, I.M., 2009. Petrogenesis of Late Mesozoic mafic dykes in the Jiaodong Peninsula, eastern North China Craton and implications for the foundering of lower crust. Lithos 113, 621–639.
Martin, C.E., 1991. Osmium isotopic characteristics of mantle-derived rocks. Geochimica et Cosmochimica Acta 55, 1421–1434.
McDonough, W.F., 1990. Constraints on the composition of the continental lithospheric mantle. Earth and Planetary Science Letters 101, 1–18.
McDonough, W.F., Sun, S.S., 1995. The composition of the earth. Chemical Geology 120, 223–253.
McKenzie, D., O'Nions, R.K., 1991. Partial melt distributions from inversion of rare earth element concentrations. Journal of Petrology 32, 1021–1091.
Meisel, T., Walker, R.J., Irving, A.J., Lorand, J.P., 2001. Osmium isotopic compositions of mantle xenoliths: a global perspective. Geochimica et Cosmochimica Acta 65, 1311–1323.
Menzies, M.A., Xu, Y.G., 1998. Geodynamics of the North China Craton. In: Flower, M., Chung, S.L., Lo, C.H., Lee, T.Y. (Eds.), Mantle dynamics and plate interactions in East Asia: American Geophysical Union, 27, pp. 155–165.
Menzies, M.A., Fan, W.M., Zhang, M., 1993. Palaeozoic and Cenozoic lithoprobes and the loss of >120 km of Archaean lithosphere, Sino-Korean craton, China. In: Prichard, H.M., Alabaster, T., Harris, N.B.W., Neary, V.R. (Eds.), Magmatic Processes and Plate Tectonics. : Geological Society, 76. London, Special Publications, pp. 71–81.
Menzies, M.A., Xu, Y.G., Zhang, H.F., Fan, W.M., 2007. Integration of geology, geophysics and geochemistry: a key to understanding the North China Craton. Lithos 96, 1–21.
Navon, O., Stolper, E., 1987. Geochemical consequence of melt percolation: the upper mantle as a chromatographic column. Journal of Geology 95, 285–307.
Nicolas, A., 1986. Structure and petrology of peridotites: clues to their geodynamic environment. Reviews of Geophysics 24, 875–895.
Niu, Y.L., 2005. Generation and evolution of basaltic magmas: some basic concepts and a new view on the origin of the Mesozoic–Cenozoic basaltic volcanism in eastern China. Geological Journal of China Universities 11, 9–46.
Norman, M.D., 1998. Melting and metasomatism in the continental lithosphere: laser ablation ICPMS analysis of minerals in spinel lherzolites from eastern Australia. Contributions to Mineralogy and Petrology 130, 240–255.
Pearson, D.G., Irvine, G.J., Ionov, D.A., Boyd, F.R., Dreibus, G.E., 2004. Re–Os isotope systematics and platinum group element fractionation during mantle melt extraction: a study of massif and xenolith peridotite suites. Chemical Geology 208, 29–59.
Peslier, A.H., Reisberg, L., Ludden, J., Francis, D., 2000. Os isotopic systematics in mantle xenoliths; age constraints on the Canadian Cordillera lithosphere. Chemical Geology 166, 85–101.
Reisberg, L., Lorand, J.P., 1995. Longevity of sub-continental mantle lithosphere from osmium isotope systematics in orogenic peridotite massifs. Nature 376, 159–162.
Roy-Barman, M., Allègre, C.J., 1994. $^{187}Os/^{186}Os$ ratios of mid-ocean ridge basalts and abyssal peridotites. Geochimica et Cosmochimica Acta 58, 5043–5054.
Rudnick, R.L., Gao, S., Ling, W.L., Liu, Y.S., McDonough, W.F., 2004. Petrology and geochemistry of spinel peridotite xenoliths from Hannuoba and Qixia, North China craton. Lithos 77, 609–637.
Snow, J.E., Reisberg, L., 1995. Os isotopic systematics of the MORB mantle: results from altered abyssal peridotites. Earth and Planetary Science Letters 133, 411–421.
Sobolev, A.V., Migdisov, A.A., Portnyagin, M.V., 1996. Incompatible element partitioning between clinopyroxene and basalt liquid revealed by the study of melt inclusions in minerals from Troodos lavas, Cyprus. Petrology 4, 307–317.
Standish, J.J., Hart, S.R., Blusztajn, J., Dick, H.J.B., Lee, K.L., 2002. Abyssal peridotite osmium isotopic compositions from Cr-spinel. Geochemistry, Geophysics, Geosystems 3 http://dx.doi.org/10.1029/2001GC000161.
Sun, S.S., McDonough, W.F., 1989. Chemical and isotopic systematics of oceanic basalts: implications for mantle composition and processes. In: Saunders, A.D., Norry, M.J. (Eds.), Magmatism in the Ocean Basins. : Geological Society. London Special Publications, pp. 313–345.
Takazawa, E., Frey, F.A., Shimizu, N., Obata, M., 2000. Whole rock compositional variation in an upper mantle peridotite (Horoman, Hokkaido, Japan): are they consistent with a partial melting process? Geochimica et Cosmochimica Acta 64, 695–716.
Tu, X.L., Zhang, H., Deng, W.F., Ling, M.X., Liang, H.Y., Liu, Y., Sun, W.D., 2011. Application of RESOlution in-situ laser ablation ICP-MS in trace element analyses. Geochimica 40, 83–89 (In Chinese with English Abstract).
Walker, R.J., Carlson, R.W., Shirey, S.B., Boyd, F.R., 1989. Os, Sr, Nd, and Pb isotope systematics of southern African peridotite xenoliths: implications for the chemical evolution of subcontinental mantle. Geochimica et Cosmochimica Acta 53, 1583–1595.
Walter, M.J., 1998. Melting of garnet peridotite and the origin of komatiite and depleted lithosphere. Journal of Petrology 39, 29–60.
Walter, M.J., 2003. Melt Extraction and Compositional Variability in Mantle Lithosphere. In: Holland, H.D., Turekian, K.K. (Eds.), Treatise on Geochemistry: The Mantle and Core, 2. Elsevier-Pergamon, pp. 363–394.
Witt-Eickschen, G., Seck, H.A., 1991. Solubility of Ca and Al in orthopyroxene from spinel peridotite: an improved version of an empirical geothermometer. Contributions to Mineralogy and Petrology 106, 431–439.
Wu, F.Y., Walker, R.J., Yang, Y.H., Yuan, H.L., Yang, J.H., 2006. The chemical-temporal evolution of lithospheric mantle underlying the North China Craton. Geochimica et Cosmochimica Acta 70, 5013–5034.
Xiao, Y., Zhang, H.F., Fan, W.M., Ying, J.F., Zhang, J., Zhao, X.M., Su, B.X., 2010. Evolution of lithospheric mantle beneath the Tan-Lu fault zone, eastern North China Craton: evidence from petrology and geochemistry of peridotite xenoliths. Lithos 117, 229–246.
Xu, Y.G., 2001. Thermo-tectonic destruction of the archaean lithospheric keel beneath the Sino-Korean Craton in China: evidence, timing and mechanism. Physics and Chemistry of the Earth, Part A: Solid Earth and Geodesy 26, 747–757.
Xu, Y.G., Bodinier, J.L., 2004. Contrasting enrichments in high and low temperature mantle xenoliths from Nushan, Eastern China: results of a single metasomatic event during lithospheric accretion? Journal of Petrology 45, 321–341.
Xu, Y.G., Menzies, M.A., Mattey, D.P., Lowry, D., Harte, B., Hinton, R.W., 1996. The nature of the lithospheric mantle near the Tancheng–Lujiang fault, China: an integration of texture, chemistry and O-isotopes. Chemical Geology 134, 67–81.
Xu, Y.G., Sun, M., Yan, W., Liu, Y., Huang, X.L., Chen, X.M., 2002. Xenolith evidence for polybaric melting and stratification of the upper mantle beneath South China. Journal of Asian Earth Sciences 20, 937–954.
Xu, Y.G., Chung, S.L., Ma, J.L., Shi, L.B., 2004a. Contrasting Cenozoic lithospheric evolution and architecture in the western and eastern Sino-Korean craton: constraints from geochemistry of basalts and mantle xenoliths. Journal of Geology 112, 593–605.
Xu, Y.G., Huang, X.L., Ma, J.L., Wang, Y.B., Iizuka, Y., Xu, J.F., Wang, Q., Wu, X.Y., 2004b. Crust-mantle interaction during the tectono-thermal reactivation of the North China Craton: constraints from SHRIMP zircon U-Pb chronology and geochemistry of Mesozoic plutons from western Shandong. Contributions to Mineralogy and Petrology 147, 750–767.
Xu, Y.G., Ma, J.L., Huang, X.L., Iizuka, Y., Chung, S.L., Wang, Y.B., Wu, X.Y., 2004c. Early cretaceous gabbroic complex from Yinan, Shandong Province: petrogenesis and mantle domains beneath the North China Craton. International Journal of Earth Sciences 93, 1025–1041.
Xu, Y.G., Li, H.Y., Pang, C.J., He, B., 2009. On the timing and duration of the destruction of the North China Craton. Chinese Science Bulletin 54, 3379–3396.
Yang, J.H., Chung, S.L., Zhai, M.G., Zhou, X.H., 2004. Geochemical and Sr-Nd-Pb isotopic compositions of mafic dikes from the Jiaodong Peninsula, China: evidence for vein-plus-peridotite melting in the lithospheric mantle. Lithos 73, 145–160.

Yang, C.H., Xu, W.L., Yang, D.B., Wang, W., Wang, W.D., Liu, J.M., 2008. Petrogenesis of Shangyu gabbro-diorites in western Shandong: geochronological and geochemical evidence. Science in China Series D: Earth Sciences 51, 481–492.
Yaxley, G.M., Green, D.H., Kamenetsky, V., 1998. Carbonatite metasomatism in the southeastern Australian lithosphere. Journal of Petrology 39, 1917–1930.
Zhang, H.F., Sun, M., Zhou, X.H., Fan, W.M., Zhai, M.G., Yin, J.F., 2002. Mesozoic lithosphere destruction beneath the North China Craton: evidence from major-, trace-element and Sr-Nd-Pb isotope studies of Fangcheng basalts. Contributions to Mineralogy and Petrology 144, 241–253.
Zhang, H.F., Goldstein, S.L., Zhou, X.H., Sun, M., Zheng, J.P., Cai, Y., 2008. Evolution of subcontinental lithospheric mantle beneath eastern China: Re–Os isotopic evidence from mantle xenoliths in Paleozoic kimberlites and Mesozoic basalts. Contributions to Mineralogy and Petrology 155, 271–293.
Zhao, G.C., Wilde, S.A., Cawood, P.A., Sun, M., 2001. Archean blocks and their boundaries in the North China Craton: lithological, geochemical, structural and P–T path constraints and tectonic evolution. Precambrian Research 107, 45–73.
Zheng, J.P., 2009. Comparison of mantle-derived materials from different spatiotemporal settings: implications for destructive and accretional processes of the North China Craton. Chinese Science Bulletin 54, 3397–3416.
Zheng, J.P., O'Reilly, S.Y., Griffin, W.L., Lu, F.X., Zhang, M., 1998. Nature and evolution of Cenozoic lithospheric mantle beneath Shandong peninsula, Sino-Korean Craton, Eastern China. International Geology Review 40, 471–499.
Zhu, R.X., Chen, L., Wu, F.Y., Liu, J.L., 2011. Timing, scale and mechanism of the destruction of the North China Craton. Science China Earth Sciences 54, 789–797.